Integration of ambient seismic noise monitoring, displacement and meteorological measurements to infer the temperature-controlled long-term evolution of a complex prone-

Geophysical Journal International

Geophys. J. Int. (2018) **213,** 1876–1897
Advance Access publication 2018 March 6
GJI Seismology

doi: 10.1093/gji/ggy090

Integration of ambient seismic noise monitoring, displacement and meteorological measurements to infer the temperature-controlled long-term evolution of a complex prone-to-fall cliff

C. Colombero,[1] L. Baillet,[2] C. Comina,[1] D. Jongmans,[2,3] E. Larose,[2,3] J. Valentin[2,3] and S. Vinciguerra[1]

[1] *Dipartimento di Scienze della Terra, Università degli Studi di Torino, I-*10125 *Torino, Italy. E-mail: chiara.colombero@unito.it*
[2] *Université Grenoble Alpes, ISTerre, F-*38041 *Grenoble, France*
[3] *CNRS, ISTerre, F-*38041 *Grenoble, France*

Accepted 2018 March 3. Received 2018 February 28; in original form 2018 January 17

SUMMARY

Monitoring the temporal evolution of resonance frequencies and velocity changes detected from ambient seismic noise recordings can help in recognizing reversible and irreversible modifications within unstable rock volumes. With this aim, the long-term ambient seismic noise data set acquired at the potentially unstable cliff of Madonna delSasso (NW Italian Alps) was analysed in this study, using both spectral analysis and cross-correlation techniques. Noise results were integrated and compared with direct displacement measurements and meteorological data, to understand the long-term evolution of the cliff. No irreversible modifications in the stability of the site were detected over the monitored period. Conversely, daily and seasonal air temperature fluctuations were found to control resonance frequency values, amplitudes and directivities and to induce reversible velocity changes within the fractured rock mass. The immediate modification in the noise parameters due to temperature fluctuations was interpreted as the result of rock mass thermal expansion and contraction, inducing variations in the contact stiffness along the fractures isolating two unstable compartments. Differences with previous case studies were highlighted in the long-term evolution of noise spectral amplitudes and directivities, due to the complex 3-D fracture setting of the site and to the combined effects of the two unstable compartments.

Key words: Geomechanics; Seismic interferometry; Seismic noise.

1 INTRODUCTION

The prevention of hazardous effects generated from rock mass instabilities within urbanized areas represents an increasingly important task. An efficient disaster management requires the identification of the prone-to-fall compartments, followed by a suitable monitoring campaign aimed at the prediction of the final collapse. Although classical methods involving both remote sensing and *in-situ* displacement measurements have been largely and successfully applied for landslide monitoring, they are still not suitable to early forecast sudden rapid rockslides and rockfalls characterized by the absence of pre-failure macroscopic signatures. In this framework, the recognition and temporal tracking of seismic precursors to failure have been proven to offer good potentialities for early-warning purposes in natural rock slopes. Beside identification, classification and location of failure-related microseismic signals (e.g. Spillmann *et al.* 2007; Lacroix & Helmstetter 2011; Lévy *et al.* 2011), ambient noise techniques have been recently applied to infer the dynamic response of potentially unstable rock slopes, showing the capability to detect both reversible and irreversible modifications in the stability of these compartments. Several ambient noise monitoring studies (e.g. Lévy *et al.* 2010; Burjánek *et al.* 2012; Bottelin *et al.* 2013a) were focused on the identification of frequency peaks within the spectral content of the recorded seismic noise. In analogy with a simple oscillator, which is characterized by a resonance frequency f_r, increasing with the stiffness K and decreasing with the mass M of the system, following:

$$f_r = \frac{1}{2\pi}\sqrt{\frac{K}{M}}, \tag{1}$$

unstable rock volumes may exhibit spectral amplifications at given frequencies, which can be directly linked to resonance phenomena. This hypothesis is supported by the absence of similar peaks in the noise spectra measured on the stable rock mass. In particular, the amplified frequency values are expected to decrease with the mass and increase with the stiffness of the unstable block and of the rock bridges connecting it to the stable cliff (Bottelin *et al.* 2017). This relationship offers a unique early-warning tool to track changes within

the unstable compartments: a loss in the contact stiffness, causing the irreversible decoupling of the unstable volume from the stable rock mass, will result in a clear drop of the resonance frequency values (Lévy *et al.* 2010). All the cited studies found the highest spectral amplification at the lowest frequency peak (first resonance frequency) followed by higher modes with progressively decreasing spectral amplitudes. Additionally, Moore *et al.* (2011), Burjánek *et al.* (2012) and Bottelin *et al.* (2013a) found clear spatial directionality for the resonance frequencies measured on prone-to-fall compartments and landslide-prone slopes. In case studies related to hard-rock slopes with simple fracture settings, the first vibration mode often revealed to be oriented perpendicularly to the main open fractures separating the unstable compartment from the stable rock mass, clearly highlighting the strong fracture control on the stability of these sites. The second vibration mode was directed perpendicularly to the first one, while the third one generally involved more complex torsional components.

Beside irreversible damaging processes, some studies revealed that the resonance frequencies also exhibit significant reversible variations controlled by weather conditions. On an unstable rock column, Lévy *et al.* (2010) found that an air temperature variation of 20 °C had generated a coherent reversible change of about 5 per cent in the value of the first resonance frequency. By contrast, when the temperature fell below zero, after or during precipitations, the resonance frequency contemporarily dramatically increased. This effect probably resulted from the formation of ice, which could have partially filled the open cracks, thus temporarily increasing the contact stiffness between the column and the stable rock mass. Bottelin *et al.* (2013b) observed coherent resonance frequency fluctuations driven by thermomechanical control on a 1000-m^3 unstable rock column. At the daily scale, in-phase fluctuations of the resonance frequency with air temperature were interpreted as the result of rock mass thermal expansion and contraction, inducing reversible closing and opening of rear fractures. At the seasonal scale, a delay of around three months was noted between the two measured parameters, probably indicating a major thermal influence on the rock bulk elastic properties rather than on the stiffness of rock bridges.

Beside spectral techniques, cross-correlation of ambient seismic noise can highlight possible seismic velocity changes within the investigated medium (Larose *et al.* 2005). Theoretical and experimental studies have shown that the cross-correlation of diffuse wavefields (e.g. ambient noise and scattered *coda* waves) can provide an estimate of the Green's function between a pair of stations, as if one of them was an active source (e.g. in Weaver & Lobkis 2001; Derode *et al.* 2003; Shapiro & Campillo 2004; Snieder 2004; Wapenaar 2004; Paul *et al.* 2005; Sabra *et al.* 2005). Since the drop in the rigidity of the investigated medium, causing slope failure, induces a negative velocity variation, also this method can be potentially used for monitoring purposes. Few applications on soft-rock gravitational instabilities are already reported in literature. Mainsant *et al.* (2012) demonstrated that seismic velocity variations, obtained from daily cross-correlation of ambient seismic noise recorded on a small active clayey landslide, are an efficient tool to predict its reactivation. Larose *et al.* (2015) verified that ambient noise cross-correlation is sensitive to hydrometeorological conditions on a sandstone landslide. Particularly, velocity changes within the unstable body were found to be strongly correlated to water-table fluctuations.

In this study, we applied both spectral and cross-correlation techniques to the long-term ambient seismic noise monitoring data set recorded at the unstable cliff of Madonna del Sasso (NW Italian Alps) between 2013 November and 2016 February. The presence of resonance phenomena within the unstable volumes of the site were already assessed in Colombero *et al.* (2017). The present work is focused on the temporal evolution of the detected resonance phenomena, with the aim of recognizing either irreversible or reversible modifications within the rock mass eventually leading to failure. Particularly, daily and seasonal variations in the resonance frequency values, related spectral amplitudes and directivities were analysed as a function of the external meteorological factors potentially controlling the stability of the site. In addition to ambient noise spectral parameters, cross-correlation was complementary applied to highlight possible velocity changes in the rock mass and confirm the temporal evolution of the rock mass behaviour. Results of both methods were finally compared to displacements measured at the site during previous or ongoing monitoring campaigns, involving crackmeters, extensometers and topographic measurements.

2 TEST SITE

The unstable cliff of Madonna del Sasso consists of a massive granitic outcrop with free high vertical faces (of approximately 150 m) on its northern, southern and eastern sides, located on the western shore of the Orta Lake, in the northwestern Italian Alps (Figs 1a and b). The upper part of the outcrop is heavily affected by open and pervasive fractures delimiting two prone-to-fall compartments (A and B in Figs 1c and d) having estimated volumes of 6000 and 6300 m^3, respectively. The two compartments are separated by the subvertical fracture F2 (355/80, dip direction/dip in degrees from N and horizontal plane, respectively) having an approximate open depth of 15 m, and are truncated at the base by the low-dipping fracture F3 (153/15). Fractures F1 (113/65) and $F4_1$ (52/80) separate the back of the two compartments from the stable cliff. In particular, fracture $F4_1$ shows an evident displacement step on the panoramic square located at the top of the cliff, with an open depth found to be approximately 16 m, both from direct observations and seismic investigations (Colombero *et al*. 2016, 2017). A minor fracture subparallel to $F4_1$ ($F4_2$, 52/80), without clear external evidences, was highlighted by seismic prospecting at the site at a distance of approximately 8 m from $F4_1$, towards the lake. Its depth was estimated at approximately 8 m from both seismic surveys and numerical simulations (Colombero *et al.* 2017).

A possible rockslide involving these unstable compartments represents a serious hazard for the houses, factories, roads and human activities located at the bottom of the slope, between the cliff and lake shore, in the Municipality of Alzo (Fig. 1b). For this reason, several monitoring techniques have been attempted at the site in the last 30 yr. Since 1981, periodic warnings related to crack openings and ground displacements have been historically reported for compartment A. Due to these past evidences and to the orientation of fractures, originating a small inclined support base for this volume and pre-disposing it to both planar and wedge sliding, monitoring measures were always focused on the only compartment A.

During 1991–1992, a network of 10 automatic crackmeters coupled with temperature probes was operating at the site to monitor the displacements of this block. Five sensors were deployed on the northern face, at different heights along fracture F1, while the others were placed on the southern face, along fracture F2. Monitoring results suggested partially reversible seasonal opening/closing of these fractures driven by air temperature fluctuations (Regione Piemonte 1993). Maximum fracture openings were recorded in winter and linked to the rock mass thermal contraction, while minimum openings in summer were related to thermal

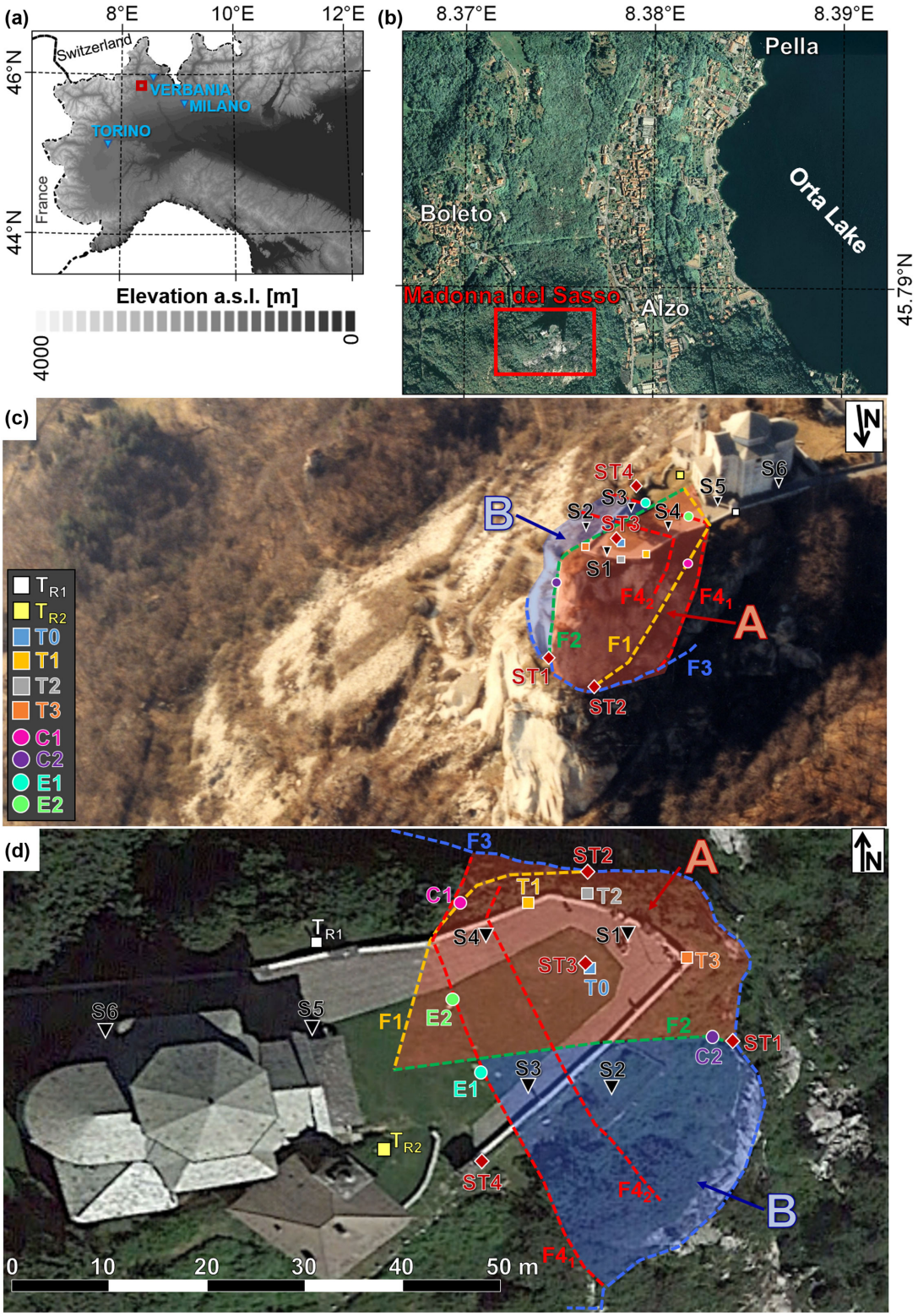

Figure 1. (a) and (b) Geographical location of the test site (red square), in the NW Italian Alps, on the western shore of the Orta Lake. (c) Northern aerial view and (d) planar view of the site. Fracture traces delimiting the unstable compartments A (in red) and B (in blue) are highlighted with dashed lines (F1–F4). Circles (C): crackmeters (1991–1992). Circles (E): wire extensometers (2007–2008). Squares (T): topographic monitoring network, ARPA Piemonte (2006–2016).Triangles (S): temporary ambient noise survey, ISTerre-Grenoble (2010 November 25–26). Diamonds (ST): long-term microseismic monitoring stations.

expansion. The highest displacement rates (>3 mm yr^{-1}) were recorded at the uppermost probes C1 and C2 (Fig. 1c), suggesting a foot constraint (along F3) on the block motion. In addition, two wire strain gauges were installed on the top yard across fracture $F4_1$ in 2007. They were discontinuously operating until 2009 July, when this monitoring system was destroyed by lightning. The available data for that period confirmed however the seasonal fluctuation of opening and closing of the fractures (data courtesy of ARPA Piemonte, Regional Agency for Environmental Protection). Since 2006, ARPA Piemonte has additionally started a topographic monitoring of the site. The topographic network (Figs 1c and d) is made up of four monitoring points located on the unstable compartment A (T0–T3) monitored from two reference stations located outside the prone-to-fall cliff (T_{R1} and T_{R2}). Measurements are discontinuously carried out on average twice a year. No alarming acceleration in the displacements is observed, but accumulating residual displacements of approximately 2 mm yr^{-1} in ENE direction (perpendicularly to $F4_1$) and −2.7 mm yr^{-1} along the vertical plane are measured. The adopted techniques were all mainly devoted to the monitoring of displacements across the open fractures rather than on the search for failure precursors, and all suffered from limitations imposed by both site morphology and difficulties in continuous recording operations. Despite no relevant irreversible changes were detected in the last 30 yr, the need of a durable continuous monitoring system is still a key issue for the site, due to the progressive accumulation of residual displacements. Local people's awareness of the risk related to the site is also increasing over years, particularly in occasion of isolated phenomena (e.g. in winter 2013 and spring 2015) when several damages and confined collapses occurred in the panoramic square at top of the cliff. After a period of intense rainfalls (2015 March–April), opening depths of more than 12 m were directly measured in localized open chasms generated along the near vertical fractures $F4_1$ and F2. At these locations, intense upward flows of cool air confirmed the deep persistence and opening of the two fractures. Consequently, a microseismic monitoring network of four triaxial geophones (nominal frequency = 4.5 Hz, sensitivity = 44 V (m s^{-1}) $^{-1}$) was installed at the cliff in late 2013, to test the potentiality of passive seismic methods in the recognition of seismic precursors to failure and to provide long-lasting early-warning perspectives to the monitoring of the site. Two stations were deployed on sheltered areas of the high cliff faces, at a height of approximately 45 m below the top yard, on the southeastern (ST1) and northern (ST2) sides of the unstable compartment A. The other two stations were located in shallow manholes accessible from the panoramic square, on top of the unstable compartment A (ST3) and outside the prone-to-fall part of the cliff (ST4). The four stations (Figs 1c and d) were connected to a 12-channel acquisition instrument (Granite, Kinemetrics). Power supply (12 V) was directly provided by the connection to the power line of the site. An external backup battery worked as a buffer and provided energy in case of power outage. The system was completed by a Global Positioning System (GPS) antenna, for timing and synchronization of the acquired seismic traces. Wireless data transmission was set to simplify remote system configuration, control and data download. The network was planned to operate simultaneously both in continuous (250-Hz sampling frequency) and trigger (1-kHz sampling frequency) mode. The first configuration provided continuous recordings of ambient seismic noise divided in 1-hr files, for a total of 8816 hr recorded between 2013 November and 2016 February on each channel of the monitoring network. The adopted network geometry resulted in a single station (ST3) placed at the top of the unstable compartment A, with no information related to compartment B. To implement the analysis on noise spectral features and directivity on both compartments, as a function of fracture orientations, a temporary ambient seismic noise monitoring campaign of ISTerre-Grenoble was used. During this survey, six triaxial stations (Lennartz LE3-D 5 s, S1–S6 in Figs 1c and d) were continuously recording at the site for 15 hr, on the night between 2010 November 25 and 26. Stations S1 and S4 were placed on the top of compartment A, with S1 close to the long-term microseismic station ST3. Spectral results on S1 and ST3 gave fully comparable results in terms of values, orientations and amplitudes of the noise frequency peaks, thus allowing for a reliable combination of the two data sets, as demonstrated in Colombero *et al.* (2017). In addition, S2 and S3 were recording at the top of compartment B, thus enlarging information to this compartment. The remaining stations (S5 and S6) were installed near the church, on the stable cliff.

3 METHODS

3.1 Spectral analysis of ambient seismic noise

Spectral analysis of the long-term noise recordings was undertaken to evaluate the performance of the monitoring network, recognize the presence of natural resonance frequencies in the noise spectral content and study their temporal evolution.

First, the power spectral density (PSD) of the 8816 hr of the noise data set was computed following Bendat & Piersol (1971) and McNamara &Buland (2004). Data clipping was used to reduce the influence of episodic energetic events, using an adaptive threshold fixed at four times the standard deviation of the whole detrended and demeaned signal. To further reduce the variance of the final PSD estimates, each 1-hr record was then windowed into shorter non-overlapping segments of 100 s and tapered with a 10 per cent cosine function. PSDs were then computed on each 100-s window and averaged over each 1-hr recording, after correction for the loss of amplitude due to tapering (Bendat & Piersol 1971). For each channel, resulting hourly PSDs were compared with the new high and low noise models (NHNM and NLNM) of Peterson (1993) for a global estimate of the recorded data quality.

Additionally, spectral ratio computations were performed to enhance the presence of frequency peaks in the spectral content of the recorded noise traces, following Burjánek *et al.* (2010, 2012) and Valentin *et al.* (2016). Each 1-hr recording was pre-processed following the PSD procedure (i.e. data clipping, windowing in 100-s segments and tapering). For each 100-s segment, the fast Fourier transform (FFT) was then computed. Resulting spectra were smoothed (following Konno & Ohmachi 1998; bandwidth coefficient $b = 40$) and used to compute the spectral ratios on a single station (H1/V1, H2/V2, H3/V3 and H4/V4) or between stations placed on the unstable compartment A (ST1, ST2 and ST3) and the stable reference one (ST4). The horizontal resultant spectrum H_f was obtained from the spectra of the east (E_f) and north (N_f) components, as:

$$H_f = \sqrt{E_f^2 + N_f^2}. \quad (2)$$

The results were finally averaged over 1-hr periods. Since PSD and spectral ratio procedures led to 8816 hourly results for each component of the four monitoring stations, probability density functions (PDFs) of both data sets were computed for each recording channel, using linearly spaced bins of 0.1-Hz frequency length and 1-dB power amplitude. In addition, the related temporal evolutions

were further analysed to distinguish anthropic and natural frequencies of the site.

The 3-D spatial directivity of these spectral peaks was already investigated in Colombero *et al.* (2017) as a function of the orientation of the main fractures confining the unstable volumes. In this study, the long-term temporal variation of directivity was complementary analysed. For each 1-hr recording, the frequency distribution (in the 1–10-Hz range) and the related vibration azimuth in the horizontal plane were calculated from the composition of the average E and N spectra, obtained from FFT computation. Similarly, composing the horizontal spectrum corresponding to the direction of maximum vibration energy with the vertical spectrum of the same recording hour, the full 3-D orientation of the spectral peak was obtained. ISTerre-Grenoble temporary noise recordings were used in addition to the long-term stations to retrieve the vibration directions of both unstable compartments. Analysing the temporal evolution of directivity for the stations placed on compartment B was however impossible, due to the absence of long-term noise recordings. The temporal evolution of frequency values, related spectral amplitudes and vibration orientations was therefore analysed for the only compartment A as a function of the external factors potentially influencing the stability of the site (temperature and rainfalls). Based on these results and on the available temporary data, the temporal behaviour of compartment B was however hypothesized.

3.2 Cross-correlation of ambient seismic noise

Noise cross-correlation was used to complement spectral results in monitoring short- and long-term variations of the seismic properties within the unstable cliff.

Theoretically, in the case of a homogeneous velocity change dV between two stations, the noise cross-correlograms computed between these two sensors after the perturbation are expected to be shifted in time by a factor dV/V (Larose *et al.* 2015). The basic requirement for the reconstruction of surface waves is that noise sources must be uncorrelated in time and located all around the receivers (Curtis *et al.* 2006; Sato 2009; Larose *et al.* 2015). The presence of subsurface interfaces or discontinuities positively compensates for the above conditions (Weaver & Lobkis 2001; Paul *et al.* 2005; Hadziioannou *et al.* 2009).

Following the previous application on a landslide of Mainsant *et al.* (2012), cross-correlation analyses were focused in the 2–20 Hz frequency band. The processing procedure basically followed the standard methods for cross-correlation described in Bensen *et al.* (2007). As a first processing step, the Fourier spectra of the 1-hr recordings were normalized to each-frequency absolute value (spectral whitening or frequency normalization) to ensure a similar statistical contribution for all the frequencies in the bandwidth of interest (2–20 Hz). A clipping window with a cosine transition from 0 (outside the 2–20 Hz range) to 1 (inside the 2–20 Hz range) was then applied to the whitened data (amplitude normalization) to minimize the possible presence of large-amplitude events within the noise recordings.

Cross-correlograms are often computed between two-station vertical components, but the related insufficient data quality (see Section 4.1) led us to prefer the horizontal components. Consequently, 8816 hourly correlograms were then calculated using the E and N pre-processed traces of station pairs. In order to obtain more stable results with time, 409 daily E and N correlograms were computed averaging the hourly correlograms within the days in which at least 20 hr of complete recordings were available. This double computation also potentially allowed focusing both on short-time changes (daily variations) and on long-time fluctuations (seasonal variations).

All the correlograms were then filtered at subsequent central frequencies (f_c) from 3 to 19 Hz, with a 2-Hz bandwidth. For each 2-Hz band, the velocity change dV/V with respect to a reference waveform h_{ref} (the average of all the considered correlograms) was computed with the stretching technique (Sens-Schönfelder & Wegler 2006; Hadziioannou *et al.* 2009). By resampling the hourly or daily correlograms in time (t), the method tests several possible dV/V to find the one maximizing the correlation coefficient CC:

$$CC\left(\frac{dV}{V}\right) = \frac{\int h\left(t\left(1+\frac{dV}{V}\right)\right) h_{\mathrm{ref}}(t)\,dt}{\sqrt{\int h\left(t\left(1+\frac{dV}{V}\right)\right)^2 dt \int h_{\mathrm{ref}}(t)^2\,dt}}. \quad (3)$$

4 RESULTS

4.1 Spectral analysis of ambient seismic noise

Noise hourly averaged PSDs of the E, N and V channels of ST3 (unstable compartment A) and ST4 (stable reference station) are shown in Figs 2 and 3, respectively (PDFs of the whole data set in panels a, b, c and related periodograms in d, e, f). Periods with no monitoring data are related to inefficient power supply to the system. In particular, the main lacking window (2014 August–2015 April) was caused by the breakdown and consequent necessary manufacturer repair of the acquisition instrument.

From PDFs, it is highlighted that the adopted geophones are almost insensitive below 2–2.5 Hz. Above this threshold, seismic noise shows however good spectral response and variability on all the horizontal components and properly fits the range described by the NLNM and NHNM boundaries of Peterson (1993). Nevertheless, vertical components demonstrated weak (Figs 2c and 3c) and discontinuous (Figs 2f and 3f) response over the monitored period. In particular, V3 seems not correctly recording in the period 2014 January–June (Fig. 2f) and V4 shows good-quality data only in the first four monitored months (Fig. 3f), for the considered frequency band (1–10 Hz).

However, a first evident spectral peak is highlighted in the horizontal PSDs of ST3 at approximately 3 Hz ($f1$), clearly visible especially on N3 (Fig. 2b). At higher frequencies, other two spectral peaks are notable, centred around 4 Hz ($f2$) and 5.5 Hz ($f3$). On N3, $f3$ shows a spectral amplitude slightly lower than $f1$ (Fig. 2b), while on E3 (Fig. 2a), the opposite is observed; spectral amplitude of $f2$ is lower than $f1$ and $f3$ on N3, while it is more clearly detectable on E3.

PSD results on the horizontal components of ST4 (Fig. 3) weakly remark the same spectral peaks, with considerably lower spectral amplitudes. ST4 can be therefore considered as a reference stable station, even if some influences due to its proximity to the unstable compartments are still present in the data. The presence of clear spectral peaks on ST3, which are not equally well defined on the reference station ST4, is the first clue to consider $f1$, $f2$ and $f3$ as resonance frequencies of the unstable cliff. The temporal evolution of the spectral content confirms this hypothesis. In Figs 2 and 3(d–f), spectral peaks affecting extremely narrow frequency bands and not exhibiting amplitude or frequency variations over time (e.g. 5.3, 6.4, 6.8, 8 and 8.5 Hz) likely originate from continuously working machineries of industrial/energetic plants located in the surroundings of the site. Conversely, spectral peaks manifesting oscillations

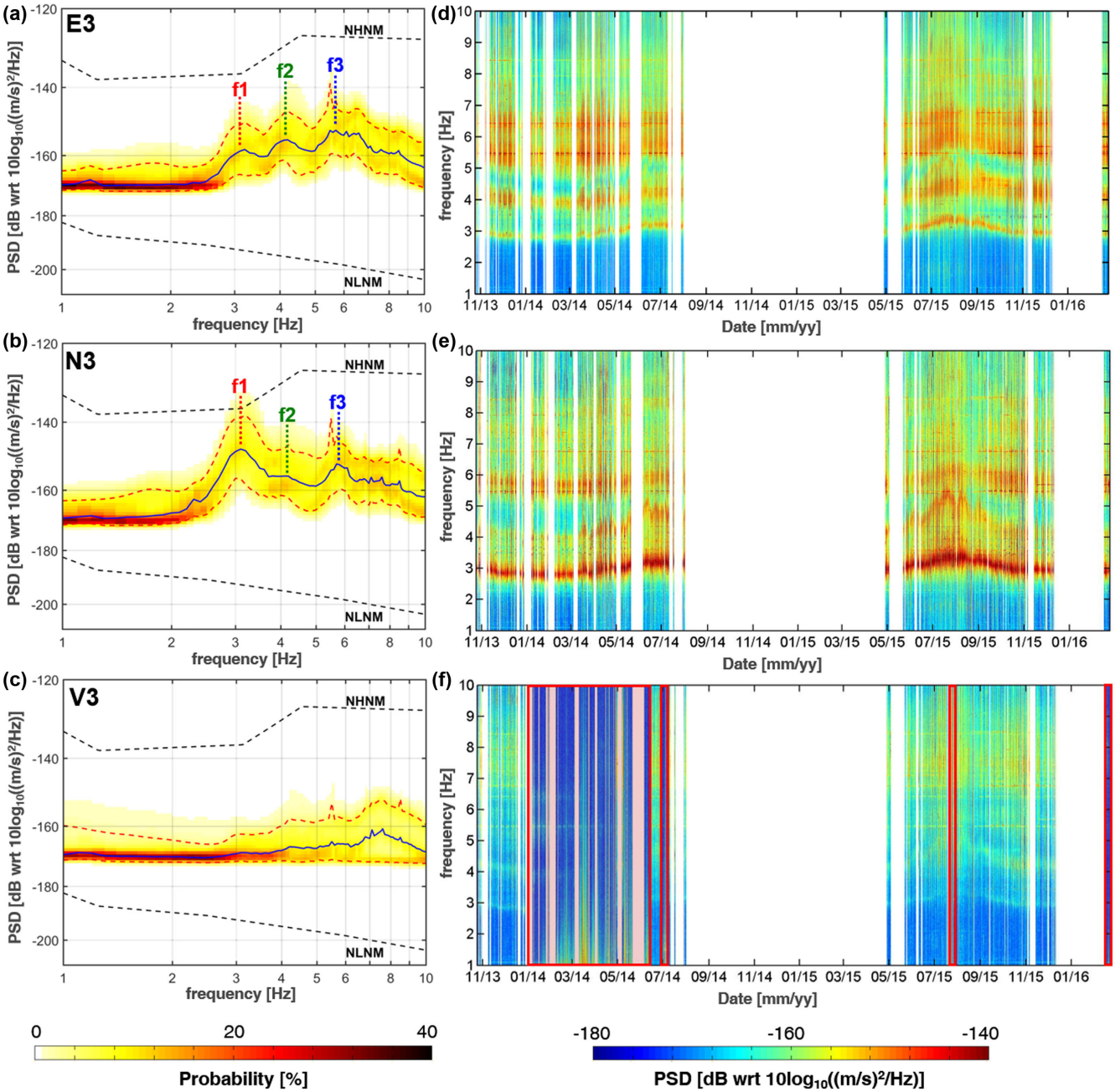

Figure 2. (a)–(c) Probability density functions of the 8816 hourly averaged power spectral densities recorded at ST3 (top of unstable compartment A), with average (blue line) and 10th–90th percentiles (red dashed lines) of the data set: (a) east, (b) north and (c) vertical components. Black dashed lines: boundaries of the NHNM and NLNM of Peterson (1993). Vertical dashed lines highlight the first three detected spectral peaks ($f1$, $f2$ and $f3$). (d)–(f) Hourly averaged power spectral densities of ST3 over the whole monitored period: (d) east, (e) north and (f) vertical components. In (f), red windows highlight periods with insufficient vertical data quality.

within the period are considered as natural frequencies of the site. These fluctuations are centred around 3, 4 and 5.5 Hz (overlapping the anthropic disturbance), which are therefore confirmed as the first three resonance frequencies of the site. In particular, the fundamental frequency ($f1$) of the site shows the highest spectral amplitude on ST3, at the top of the rock column, with values fluctuating from 2.6 Hz (winter) to 3.4 Hz (summer), and an average of 2.9 Hz over the 8816 monitored hours. The second resonance frequency ($f2$) follows the same seasonal trend, in a range from 3.8 Hz (winter) to 5.2 Hz (summer), with an average value of 4.0 Hz. The third resonance frequency ($f3$), second in order of spectral amplitude, shows marked fluctuations around the average value of 5.5 Hz in agreement with $f1$ and $f2$ trends, ranging from 5.1 Hz (winter) to 6.2 Hz (summer).

Both single station (e.g. H3/V3 in Fig. 4a) and site-reference (e.g. E3/E4 in Fig. 4b and N3/N4 in c) spectral ratios confirm and emphasize these spectral observations. The H/V spectral ratio computed on ST3 exceeds 10 at the fundamental frequency of the site ($f1$, Fig. 4a). A significant amplitude of the H/V peaks related to $f2$ and $f3$ is also found, with average values of the ratio around 4 and 6, respectively. The hierarchy in spectral amplitude (A) of the first three frequencies is thus confirmed, with $A_{f1} > A_{f3} > A_{f2}$. The

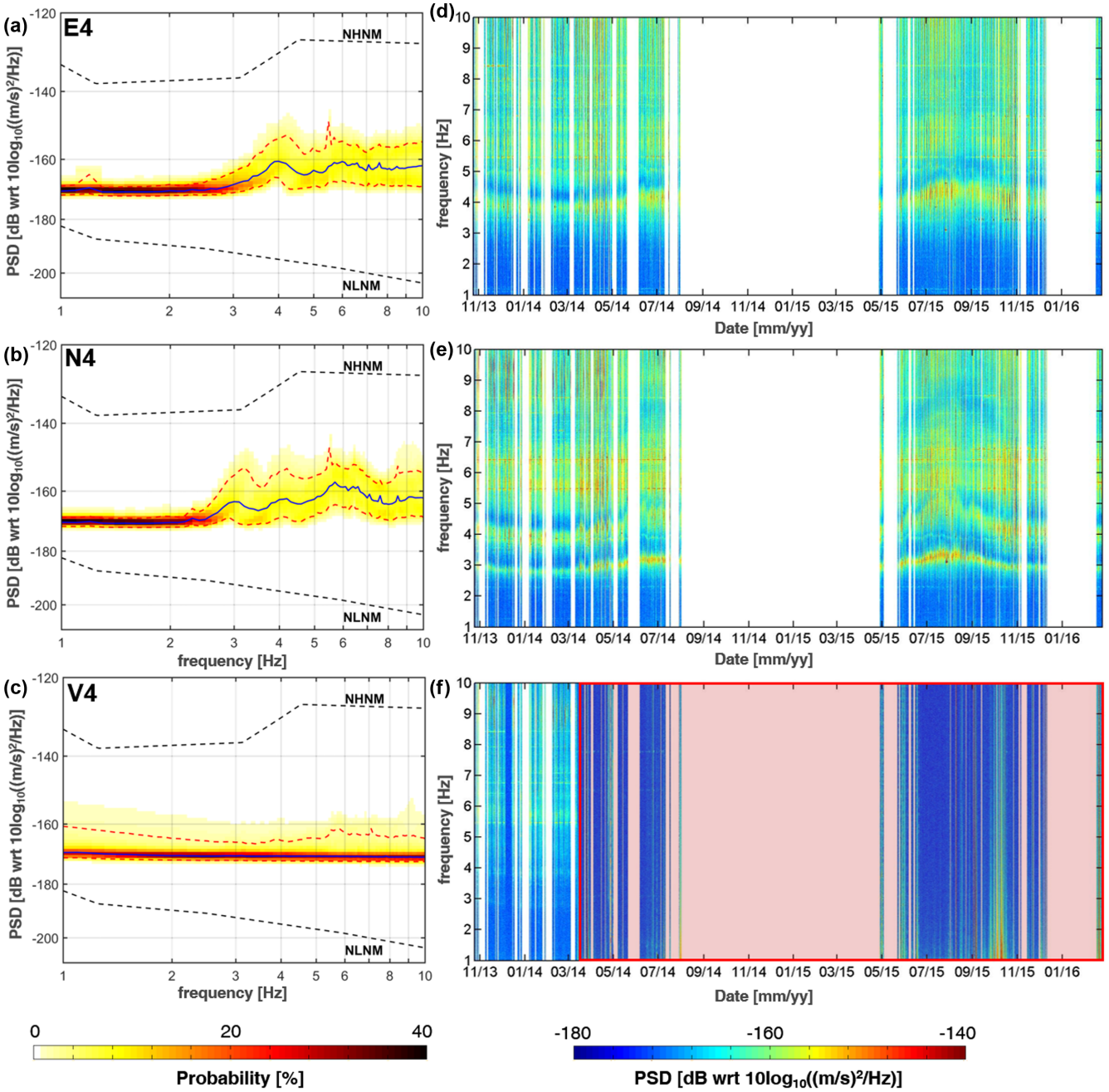

Figure 3. (a)–(c) Probability density functions of the 8816 hourly averaged power spectral densities recorded at ST4 (reference station), with average (blue line) and 10th–90th percentiles (red dashed lines) of the data set: (a) east, (b) north and (c) vertical components. Black dashed lines: boundaries of the NHNM and NLNM of Peterson (1993). (d)–(f) Hourly averaged power spectral densities of ST4 over the whole monitored period: (d) east, (e) north and (f) vertical components. In (f), red windows highlight periods with insufficient vertical data quality.

H/V maximum follows the seasonal trend already highlighted from PSDs (Fig. 4d).

The site-reference spectral ratios led to similar results (Figs 4b and c). Disregarding poor-quality vertical components significantly improved the results, allowing for a more complete and reliable temporal analysis. The first resonance frequency ($f1$) exhibits the highest values in the spectral ratios over the whole monitored period (around 10, Fig. 4c) and the most marked daily and seasonal fluctuations (Fig. 4f) on the N components. By contrast, $f2$ and $f3$ are clearer on the E components (with $A_{f3} > A_{f2}$, Fig. 4b).

To avoid errors due to the poor quality of vertical recordings, the temporal evolution of the first three resonance frequencies at ST3 was further analysed only in the horizontal plane, in terms of frequency value (Fig. 5a), maximum-energy vibration direction (Fig. 5b) and spectral amplitude (Fig. 5c). Representative 3-D orientations and spectral amplitudes for $f1$, $f2$ and $f3$ were however retrieved for all the stations (Fig. 5d), averaging the horizontal parameters over the whole period and the vertical dips only over time windows with good data quality. Only ST2 showed no usable vertical recordings over the entire monitored period to compute the related vibration dip.

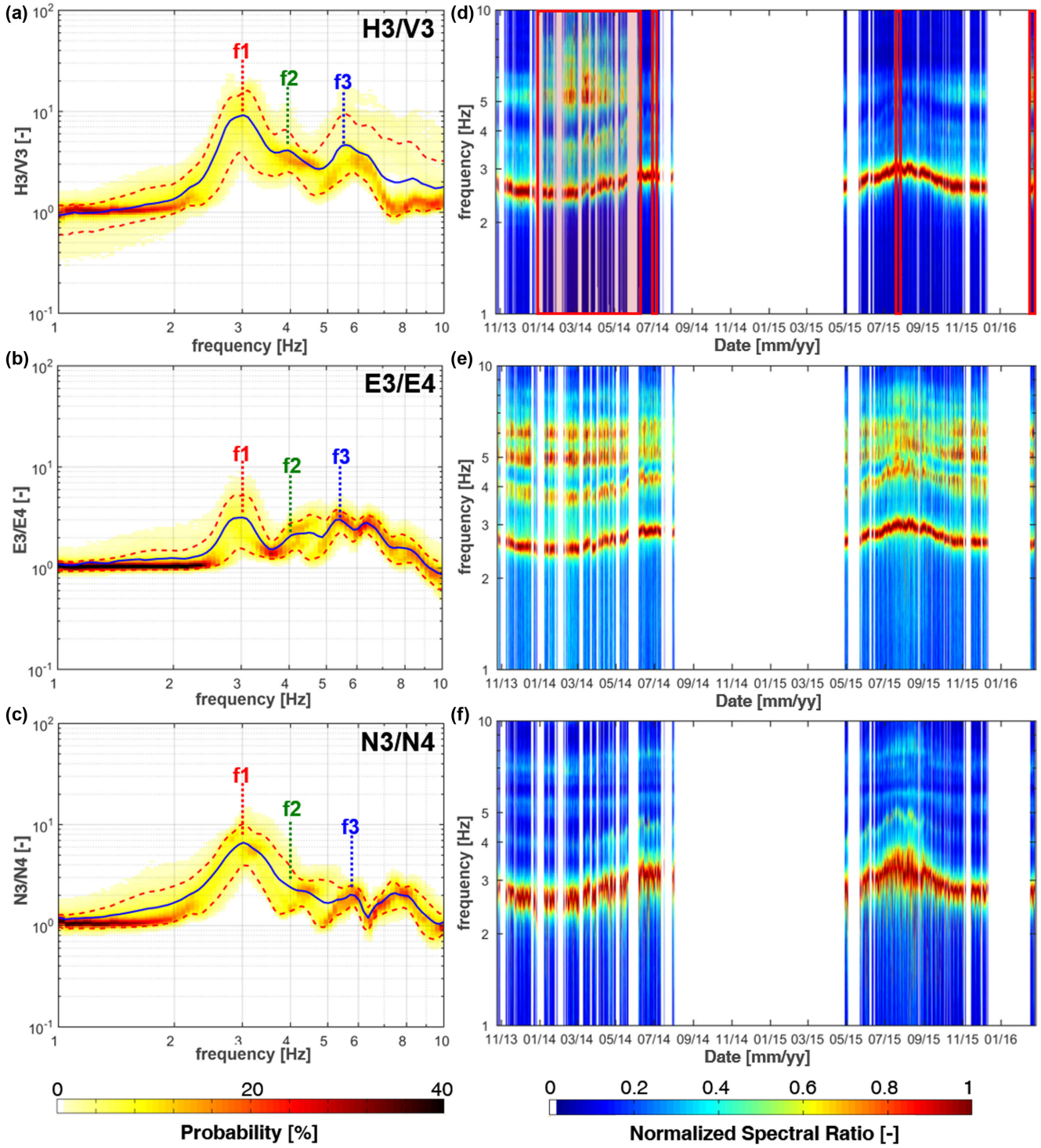

Figure 4. (a)–(c) Probability density functions of the 8816 hourly averaged spectral ratios, with average (blue line) and 10th–90th percentiles (red dashed lines) of the data set: (a) H3/V3, (b) E3/E4 and (c) N3/N4. Vertical dashed lines highlight the first three detected spectral peaks ($f1$, $f2$ and $f3$). (d)–(f) Hourly averaged spectral ratios over the whole monitored period: (d) H3/V3, (e) E3/E4 and (f) N3/N4. In (d), red windows highlight periods with insufficient vertical data quality.

The first three resonance frequencies show again the same seasonal fluctuation in the related values (Fig. 5a). Nevertheless, short-period oscillations are more marked on $f2$ and $f3$. Values around 5.3 $\pm$ 0.05 Hz were filtered out, due to the presence of the strong anthropic disturbance overlapping the natural $f3$ in this narrow frequency band (Figs 2d and e). The vibration orientation is stable for $f1$ (165°), while $f2$ and $f3$ show azimuthal fluctuations over time (Fig. 5b). From spring to summer, $f2$ tends to align to $f1$ azimuth, with values higher than 150°, while maximum divergence is found during winter, with values down to 110° from N direction. Despite the marked short-period fluctuations, $f3$ azimuthal variations reduce in the range 40°–60° in summer. In the same periods,

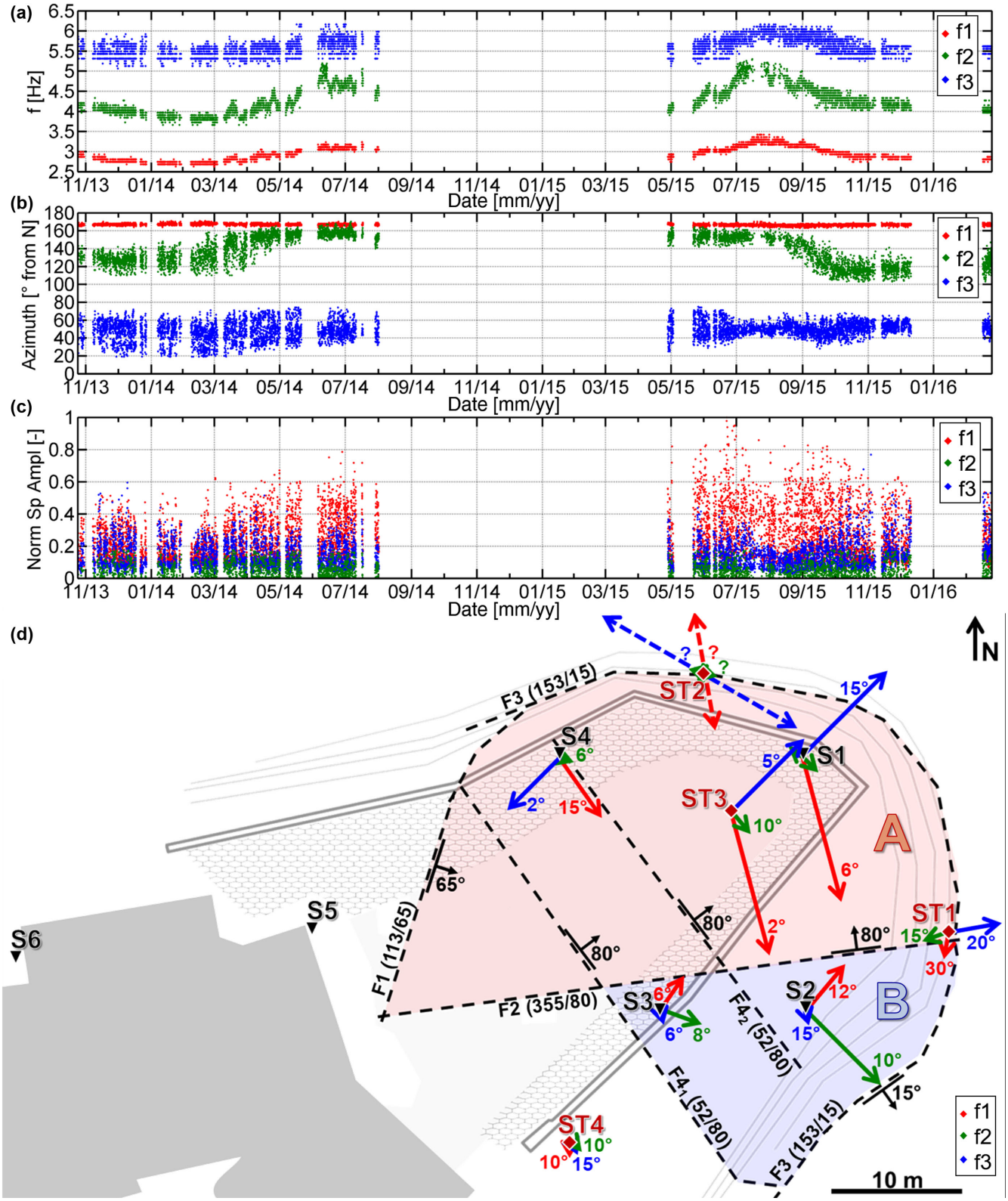

Figure 5. Temporal evolution of (a) value, (b) azimuth (in degrees from N) and (c) spectral amplitude (normalized to $f1$ maximum of the whole data set) of the first three resonance frequencies ($f1$ in red, $f2$ in green and $f3$ in blue) measured on the horizontal plane at ST3. (d) 3-D average orientation and amplitude of $f1$, $f2$ and $f3$ at all the available noise monitoring stations, modified from Colombero *et al.* (2017). The tip of each arrow marks the dip direction in the vertical plane, while the length is proportional to the related average spectral amplitude normalized to the amplitude of $f1$ recorded at S1 (for the ISTerre-Grenoble temporary survey) and ST3 (for the long-term monitoring stations). The vertical component of ST2 was not available for the computation of the dip direction (dashed coloured arrows). Fractures traces (F1–F4) are indicated in black with their related dip direction/dip.

the lowest spectral amplitude is found for $f3$ (Fig. 5c), while A_{f1} reaches the maximum. Conversely, during winter, A_{f3} higher than A_{f1} is often observed. A_{f2} is always lower than A_{f1} and A_{f3}.

Average orientations at all the available monitoring stations are summarized in Fig. 5(d) to have a global spatial understanding of the 3-D vibration dynamics of both unstable compartments. It must be noted that orientations are averaged over 8816 hr for the long-term monitoring stations (ST1–ST4) and over only 15 hr for the temporary stations (S1–S6, 2010 November 25–26). As expected, no spectral peaks and directivities were detected at stations S5 and S6, located in the stable area. Weak spectral amplifications are observed at ST4, probably due to its increased proximity to the unstable area. These observations confirm that $f1$, $f2$ and $f3$ are resonance frequencies of the prone-to-fall compartments. In the unstable area, a marked difference in $f1$, $f2$ and $f3$ orientation is noted between the stations placed on compartment A and B. The vibration pattern is much more complex than the simple modes found in previous works on nearly 2-D rock mass configurations (Lévy *et al.* 2010; Burjánek *et al.* 2012; Bottelin *et al.* 2013a; Del Gaudio *et al.* 2014). In addition, the common hierarchy in spectral amplitude ($A_{f1} > A_{f2} > A_{f3}$) detected on the cited studies is not respected on both compartment A (where $A_{f1} > A_{f3} > A_{f2}$) and compartment B, where at S2 even A_{f2} is stronger than A_{f1}, and A_{f3} is almost negligible. On both compartments, $f1$ orientation does not follow the most probable direction of collapse (as found in nearly 2-D rock columns), but seems to suggest a convergence of the two compartments. Conversely, $f2$ and $f3$ could potentially trace the collapse preferential directions of compartment B and A, respectively. On each compartment, these frequencies show indeed a relevant spectral amplitude (comparable with A_{f1}), while they are almost negligible on the other compartment.

4.2 Cross-correlation of ambient seismic noise

Long-term cross-correlation was computed for the station pair ST3 and ST4. Hourly and daily results in the first six investigated frequency bands (from 2–4 to 12–14 Hz) are completely presented in Appendix A (Figs A1 and A2). The highest correlation coefficients over time were obtained in the 2–4-Hz band, around the first resonance frequency of the site ($f1$). Increasing the central frequency of the band, correlation was progressively lost between the sensors and results became unstable over time, both for hourly and daily cross-correlograms. The interpretation of this progressive loss in correlation with increasing frequency is possibly linked to the highly attenuating and heterogeneous seismic velocity field within the fractured rock mass.

Hourly and daily cross-correlograms and computed velocity changes are therefore reported in Fig. 6 only for the lowest frequency band (2–4 Hz). A slight asymmetry in the central part of the correlograms [−0.5 s 0.5 s] is noted, particularly on the N components (Figs 6a and e), likely due to the imperfect spatial distribution of noise sources. Signals observed around time delay = 0 s correspond to waves directly traveling from the noise sources to the receivers. Since these early direct waves are very sensitive to changes in the noise source position, they were removed from the computation. Considering an average Rayleigh-wave velocity V_R of 1350 m s^{-1} in the 2–20-Hz range (from Colombero *et al.* 2017) and a distance between the two stations of 25 m, the slowest Rayleigh-wave direct arrival delay between the two sensors is approximately 0.02 s. Therefore, using the correlograms in the time intervals [−2 s −0.5 s] and [0.5 s 2 s] widely ensured to work on coda waves which have widely sampled the region around all the considered station pairs.

A significant annual velocity variation over time (±10 per cent from the average value) is found in the 2–4-Hz range between ST3 and ST4, as shown in Figs 6(c) and (g) for both hourly and daily correlograms, respectively. The related correlation coefficients CC (Figs 6d and h) are extremely high (∼0.9), particularly on the N components. In autumn and winter (from October to February), a relative decrease in the phase velocity is detected within the rock mass, while velocity values start to increase again during spring, reaching the maximum in August, for both the available monitored annual cycles. This temporal evolution mirrors the trend of resonance frequency values observed with spectral analysis. Increasing the frequency band, the phase velocity change reduces in amplitude to less than ±5 per cent (Appendix A, Figs A1 and A2) from the average value, with associated lower correlation coefficients, but it is still visible on the results.

5 DISCUSSION

5.1 Thermal control on resonance frequencies, velocity fluctuations and fracture openings

The role of environmental factors potentially affecting the stability of the site on the detected resonance frequency and velocity fluctuations was analysed. Fig. 7(a) shows the 30-min rainfall amount over the whole monitored period, while 30-min temperature measured both outside the rock mass and at 20-m depth in a borehole (located in the same shallow manhole of ST3) are reported in Fig. 7(b). For direct comparison with these meteorological data, representative results of spectral analysis and cross-correlation are summarized in Figs 7(c) and (d), respectively.

No irreversible changes with a marked sudden decrease in the resonance frequency values, resulting from irrecoverable damage processes or stiffness losses within the rock mass, are detected during the monitored period. Both temporal variations in resonance frequencies obtained from spectral analysis ($f1$ in Fig. 7c), and velocity changes detected by cross-correlation (hourly results in Fig. 7d) suggest reversible short- and long-term cycles primarily controlled by air temperature fluctuations (Fig. 7b) rather than by precipitations (Fig. 7a).

The interpretation of this temperature-related behaviour of the rock mass is supported by the thermal effects on fracture openings already highlighted from previous site monitoring with direct displacement measurements (Regione Piemonte 1993).

Cross-correlation between $f1$ values and air temperature was undertaken to quantify the time response of noise spectral features to environmental variations, both at the seasonal and daily scales. To investigate seasonal fluctuations, sine curves were least-square fitted to both air temperature and frequency data sets, after demeaning and normalization to the average values (Fig. 8a). The same procedure was undertaken to evaluate the delay between air and deep temperature measurements. Resulting sine curves oscillate of approximately ±9 per cent from the average frequency value (f_{av} = 2.90 Hz), ±68 per cent and ±32 per cent from the average air (T_{av} = 11.75 °C) and deep (T_{av} = 10.55 °C) temperatures, respectively. Cross-correlation of these sine curves gave zero delay between $f1$ and air temperature, while a delay of 55 d was found between air and deep temperatures (see location of the maxima in the cross-correlograms of Fig. 8c).

To analyse daily fluctuations, short windows with complete hourly noise recordings were cross-correlated with air temperatures,

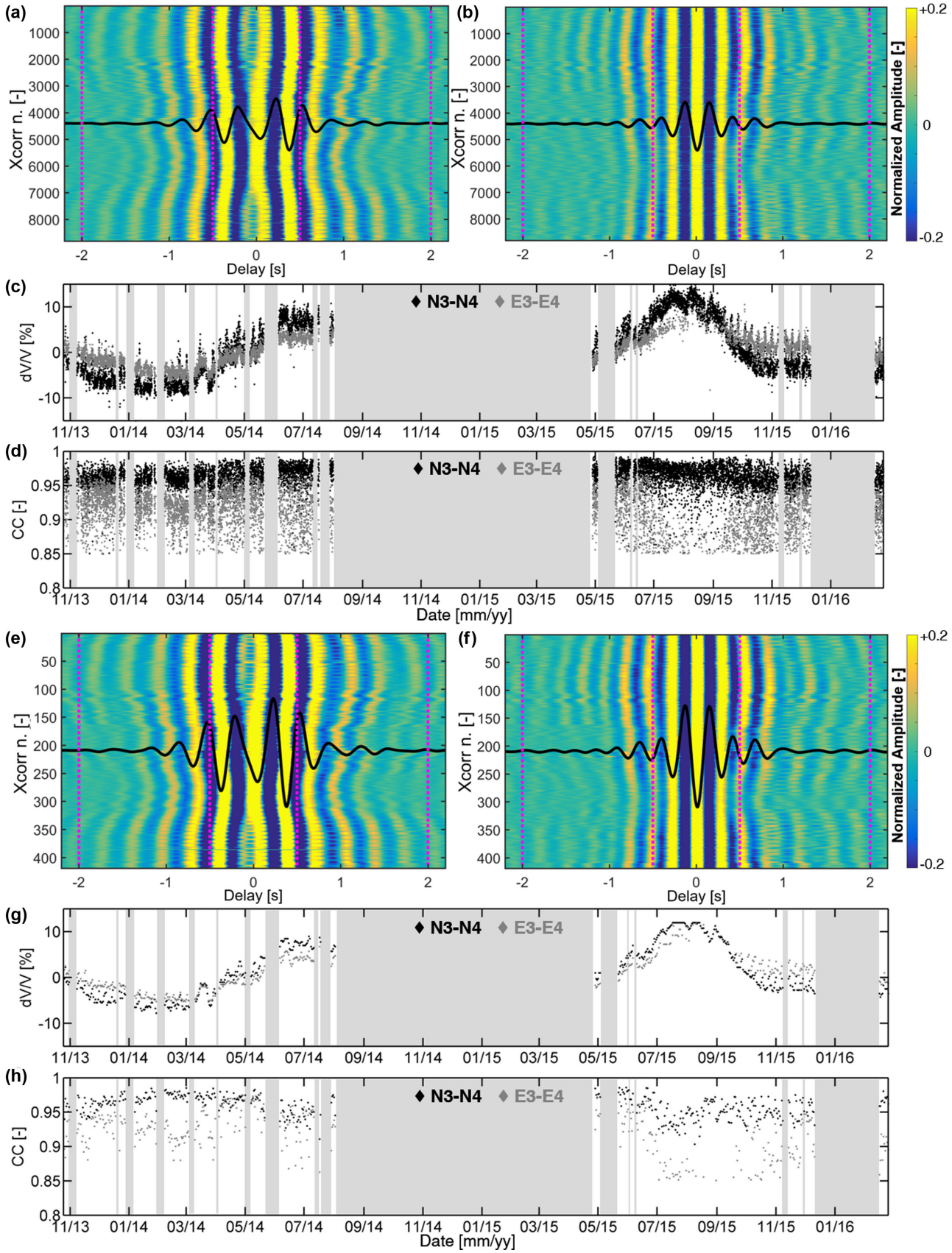

Figure 6. Cross-correlation of ambient seismic noise in the 2–4-Hz frequency band, between ST3 and ST4. (a) and (b) Hourly cross-correlograms related to (a) north and (b) east components. (c) Resulting hourly velocity changes with (d) related correlation coefficients. (e) and (f) Daily-averaged cross-correlograms related to (e) north and (f) east components. (g) Resulting daily velocity changes with (h) related correlation coefficients. In (a), (b), (e) and (f) reference correlograms are displayed in the centre by the continuous black line. Vertical dashed lines (in magenta) delimit the time intervals [−2 s −0.5 s] and [0.5 s 2 s], used for the relative velocity change estimation.

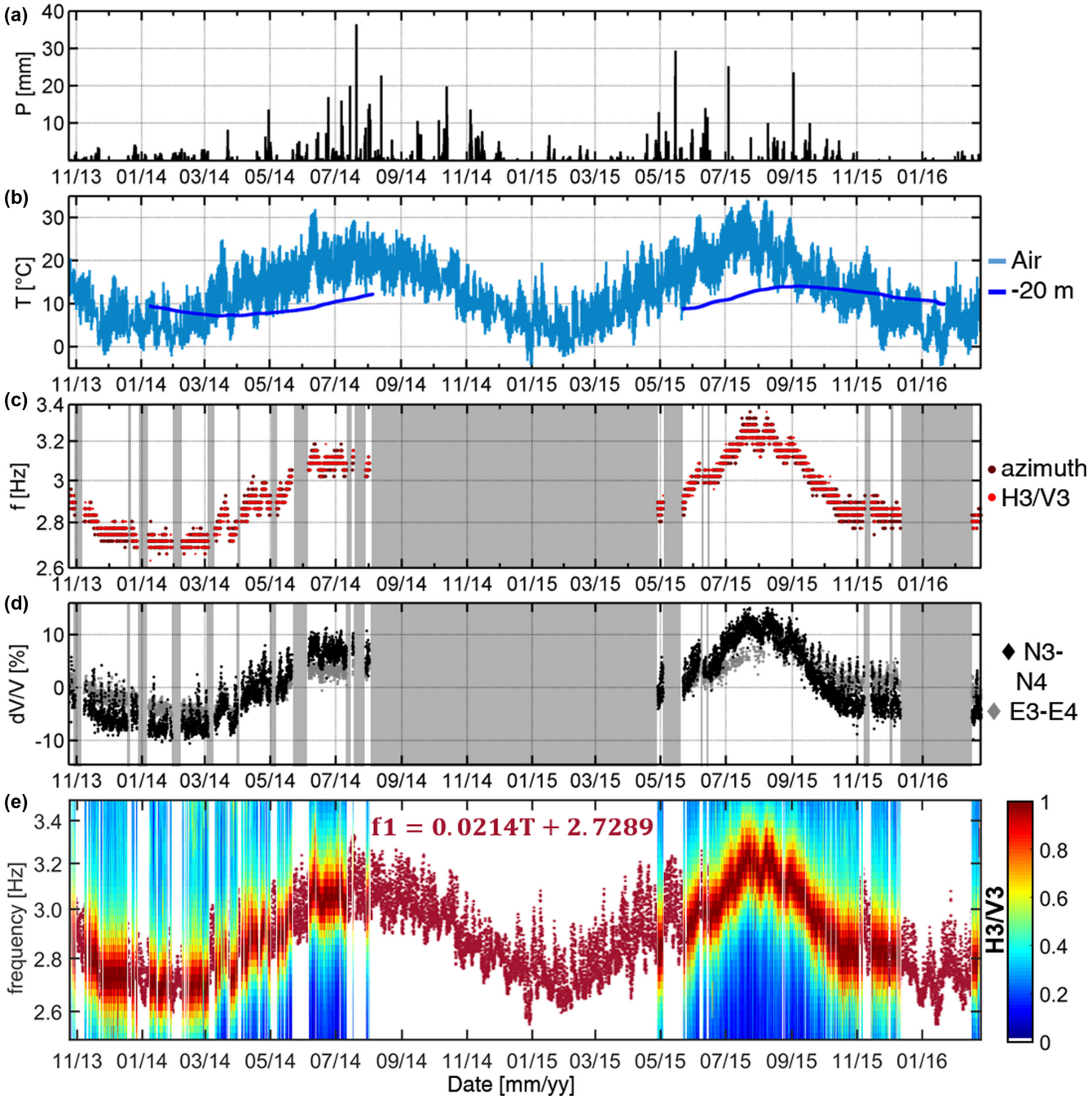

Figure 7. (a) 30-min rainfall amount and (b) 30-min air and in-hole 20-m depth temperatures recorded at the site. (c) $f1$ values hourly obtained from spectral ratios (H3/V3) and from the azimuth computation (from Fig. 5a). (d) Hourly velocity changes from ST3 and ST4 cross-correlation of the horizontal components (from Fig. 6c). (e) Zoom on $f1$ in the H3/V3 normalized spectral ratio plot (from Fig. 4d) with overlapping red dots representing $f1$ values during missing monitoring hours as calculated from the T–$f1$ linear relationship of eq. (5).

after demeaning and normalization to the average values of the data sets. Both frequency and air temperature daily variations are shown in Fig. 8(b) for a complete period of 21 d (2013 November 26–December 18). Frequency fluctuations between –5.5 per cent and +7.5 per cent and air temperatures between −137 per cent and 225 per cent from the average values ($f_{av} = 2.74$ Hz and $T_{av} = 5.07$ °C) are measured over this short period. Cross-correlation of the two parameters gave again zero delay (<1 hr, Fig. 8d).

The same in-phase behaviour was found between air temperature and velocity changes dV/V obtained from hourly and daily cross-correlation (related cross-correlograms not shown), both at the daily and seasonal scale.

The results revealed that the rock mass response to external thermal variations is immediate both on short-time (daily cycle) and on long-time (seasonal fluctuation) periods. This observation probably indicates the major contribution of fracture stiffness to the behaviour of the site, instead of a deep and pervasive thermal control on the bulk rock mass stiffness, which would have generated a delay between noise parameters and temperature (Bottelin *et al.* 2013b). Indeed, increasing temperatures induce surface rock thermal

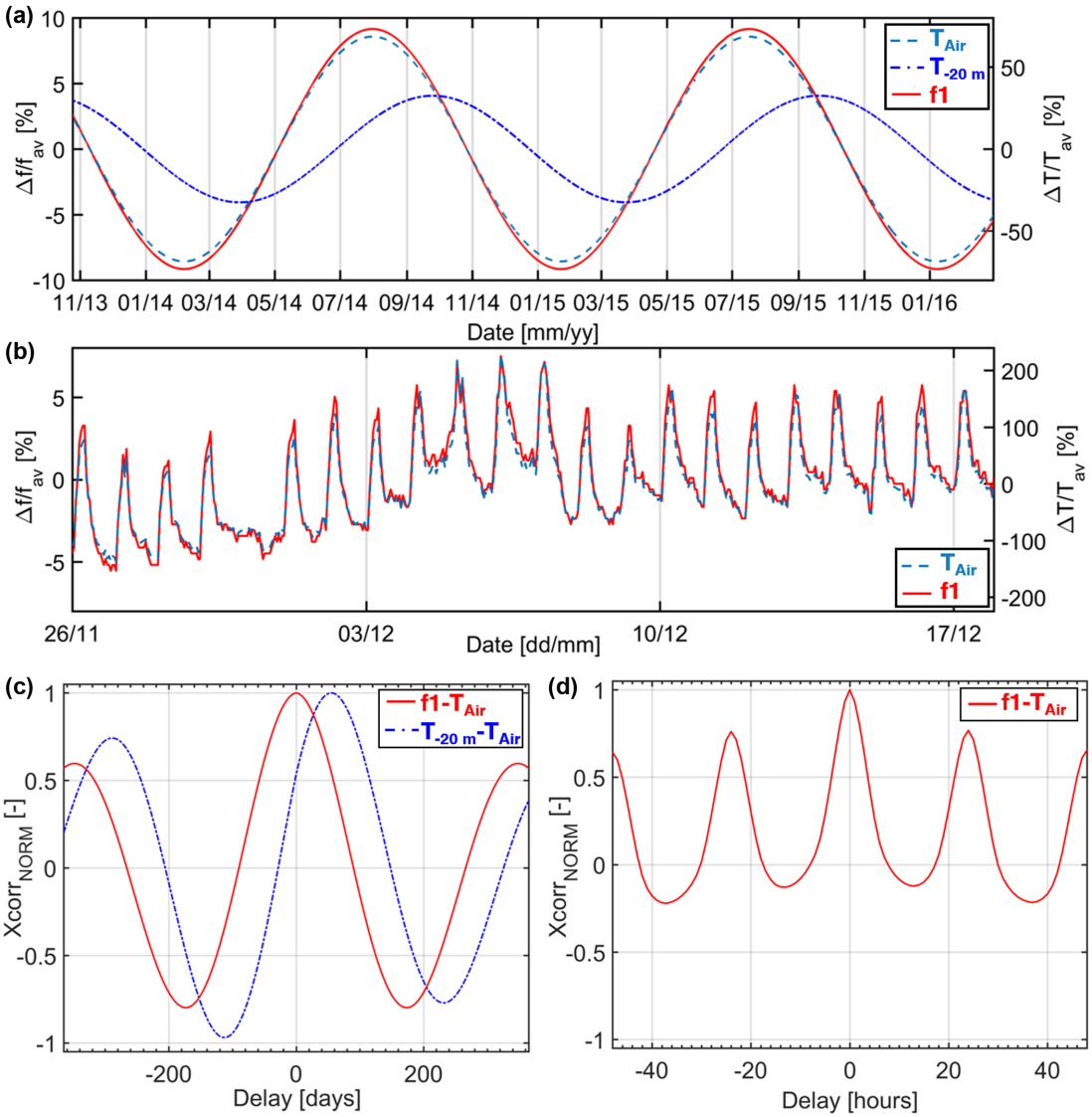

Figure 8. (a) Long-term fluctuations of frequency and temperature: least-square fitted sine curves for the first resonance frequency ($f1$), air and deep temperature measurements, after demeaning ($\Delta f = f - f_{av}$ and $\Delta T = T - T_{av}$) and normalization ($\Delta f/f_{av}$ and $\Delta T/T_{av}$) to the average values f_{av} and T_{av} of each data set, over the whole monitored period. (b) Short-term fluctuations of frequency and temperature: demeaned and normalized $f1$ and temperature variations over a short monitoring window with complete horly noise recordings (2013 November 26–2013 December 18). (c) Cross-correlograms (zoomed in the window centred around zero delay) between long-term variations of frequency and air temperature and between deep and air temperature measurements. (d) Cross-correlogram (zoomed in the window centred around zero delay) between short-term variations of frequency and air temperature.

expansion and consequent closing of microcracks near rock bridges. This increase in the contact stiffness (between the unstable compartments and the cliff) raises the resonance frequency values (Bottelin *et al.* 2013b), and generates positive velocity changes within the rock mass, as observed from cross-correlation. A decrease in air temperature generates the opposite effect, with a new opening of microcracks due to the rock mass thermal contraction and a related stiffness reduction. In addition, differential dilation between the bulk rock mass and the fracture surfaces may induce internal stresses leading to an increase in stiffness (Larose & Hall 2009; Tsai 2011), further explaining the in-phase behaviour between air temperature and resonance frequencies.

These observations are in contrast with other studies (e.g. Bottelin *et al.* 2013b) evidencing a major effect of the changes in the mechanical behaviour of the bulk rock due to long-term thermal cycles and a consequent delay of a few months between temperature changes and resonance frequency values. A decrease in the Young's Modulus (E) would be indeed expected with an increase in the temperature (T), following the linear relationship introduced by Xia *et al.* (2011):

$$E(T) = E(T_0)[1 - \theta(T - T_0)] \quad (4)$$

where T_0 is the reference temperature and θ is the temperature coefficient of Young modulus, which is material dependent. Assuming $\theta = 0.021$ (Bottelin *et al.* 2013b), a maximum decrease or increase in temperature of 20 °C from the average over the monitored period would cause an opposite 30 per cent increase or decrease in E within the rock mass and also affect the bulk rock seismic velocity. An opposite trend between resonance frequency (or cross-correlation velocity) and air temperature should therefore be expected at the

seasonal scale. In addition, if internal variations of the E modulus had been dominant in the control of the fluctuations of the natural frequencies, a delay similar or higher than the one measured between air and in-depth temperature measurements (55 d, Fig. 8c) would have probably been observed in spectral analysis and cross-correlation results. None of these considerations can be however applied to the results reported in this study.

Differences with the cited case study are most likely due to the bigger size of the unstable compartments of Madonna del Sasso (compartment volumes and minimum thicknesses are approximately six and three times greater, respectively, than in Bottelin *et al.* 2013b) making the temperature penetration less efficient on the bulk rock stiffness. In parallel, the presence of several open and persistent discontinuities amplifies the control of fracture stiffness on the stability of the site.

In order to quantify the sensitivity of the resonance frequency fluctuations to fracture opening variations, a quantitative comparison between displacement data and ambient noise results was attempted over the same 9-month period of different years. Data from crackmeters (1991 November–1992 July) and wire extensometers (2007 November–2008 July) are shown with $f1$ values over the same months of 2013–2014, in Figs 9(a)–(c), respectively, along with the related temperature fluctuations. Since the three monitoring data sets are not simultaneous, this analysis is defectively based on the assumptions of similar thermal trends during the three periods (Fig. 9d) and no significant irreversible changes in the rock mass behaviour over more than 20 yr. The direct comparison between displacements and resonance frequency (plotted together in Fig. 9e) definitively confirms the thermal control on fractures at the site, with an opposite clear trend between fracture openings and $f1$ values. It can be globally inferred that a variation in the air temperature of -10 °C induces a simultaneous opening of approximately 2 mm perpendicularly to all fractures (e.g. from November to mid-February in Figs 9a and b), resulting in a frequency drop of -0.2 Hz. In contrast, fractures slowly close with increasing temperatures. A positive variation of approximately 20 °C is needed to almost totally recover the displacements of the crackmeters placed on fractures F1 and F2 (see C1 curve, from February to late July, in Fig. 9a), while a residual displacement of 2 mm is accumulated at the extensometers placed on fracture $F4_1$ (Fig. 9c). Fracture closing is associated with a positive variation of $f1$ values ($+0.5$ Hz).

These $f1$ fluctuations are more than 10 times higher than the frequency resolution adopted for spectral analysis, and demonstrate the high sensitivity of the method to even lower-than-millimetric displacements. These results highlight the potentialities to follow reversible (and irreversible) contact stiffness changes. Consequently, a direct relationship to describe $f1$ reversible fluctuations due to air temperature (T) was inferred (and used to simulate the continuous $f1$ curve from the temperature data of Fig. 7e):

$$f1 = 0.0214\mathrm{T} + 2.7289. \quad (5)$$

with a determination coefficient $R^2 = 0.89$. This simple relationship can be used as a guiding mark for early-warning monitoring purposes at the site: once the reversible fluctuations of $f1$ (or $f2$ and $f3$) with temperature have been established, if hourly $f1$ values falling below this trend are recorded, irreversible modifications in the stiffness not driven by external factors and acceleration to failure can be immediately recognized.

5.2 Thermal control on noise spectral amplitude and directivity

Beside the described thermal control on resonance frequency values, the temporal evolution of the related spectral amplitudes and directivities was further investigated, with direct comparison between noise results and long-term topographic measurements (2006–2016, ARPA Piemonte).

The 3-D displacements of monitoring points T0 to T4 are reported in Table B1 (Appendix B), for the period between 2006 February and 2016 July. The motion at T0 (located in the same shallow manhole of ST3, Fig. 1d) is shown in the horizontal plane in Fig. 10(a) and along the vertical direction in Fig. 10(b). In 10 yr, the point moved of approximately 13 mm in ENE direction, with a total loss of height of approximately -27 mm. The topographic surveys (2 measurements per year on average) were not systematically carried out on the same dates of each years. However, periods between two subsequent measurements are likely controlled by either thermal expansion or contraction, causing fracture closing and opening, respectively. These two thermal behaviours are highlighted with two different colours in Fig. 10 and summarized in Table B2 (Appendix B) for all the monitoring points. Three periods (A–C in Fig. 10 and Table B2) are dominated by temperature increases (e.g. A, from May to October) and consequently related to thermal expansion, while seven periods (D–L in Fig. 10 and Table B2) with predominant temperature decreases (e.g. D, from October to May) are related to thermal contraction.

For each of these periods, the relative displacement from the first to the second measurement was computed along N, E and vertical directions, together with the related planar angle of orientation from N (Table B2). A direct comparison between the orientation of the resonance frequencies on compartment A (from Fig. 5d) and the displacements at all the topographic stations during the highlighted thermal expansion/contraction periods is summarized in Fig. 10(c). Even if the considered periods do not exhibit the same temporal length and distribution over years, two different preferential directions of displacement are found, related either to thermal expansion or contraction periods. During thermal expansion, displacements of compartment A are mainly oriented towards SSE (periods A–C, in Fig. 10a), thus perpendicularly to F2 (or parallel to $F4_1$) and following the basal F3 dip. During these periods, a limited loss in elevation (or even a slight increase in height) is detected (Fig. 10b). The average azimuth from N recorded at T0 is 156° (Fig. 10c). This orientation fits the direction of $f1$ measured at ST3 (dip direction/dip = 165/2; Fig. 5d).

By contrast, thermal contraction periods show a strongly different displacement orientation, taking place predominantly in ENE direction (periods D–L, in Fig. 10a), with fracture opening almost perpendicular to $F4_1$ and parallel to F2. The accumulation of residual displacement over years takes place in this direction (approximately 2 mm yr^{-1}). During these periods, displacements are more marked also on the vertical axis (approximately -3 mm yr^{-1}, Fig. 10b). The average azimuth from N recorded at T0 is 43°. This orientation is perfectly described by $f3$ average orientation at ST3 (45/5; Fig. 5d).

To further analyse the relationship between $f1$ and $f3$ on compartment A, the ratio between $f3$ and $f1$ spectral amplitudes (A_{f3}/A_{f1}) measured atST3 in the horizontal plane (from Fig. 5c) is reported in Fig. 11 for each monitored hour and compared with the air temperature curve. To follow the temporal evolution over the whole period, these spectral amplitudes (horizontal plane) were preferred to the results of H3/V3 spectral ratios, to avoid disturbances and artefacts caused by the low-quality vertical recording. Results show that

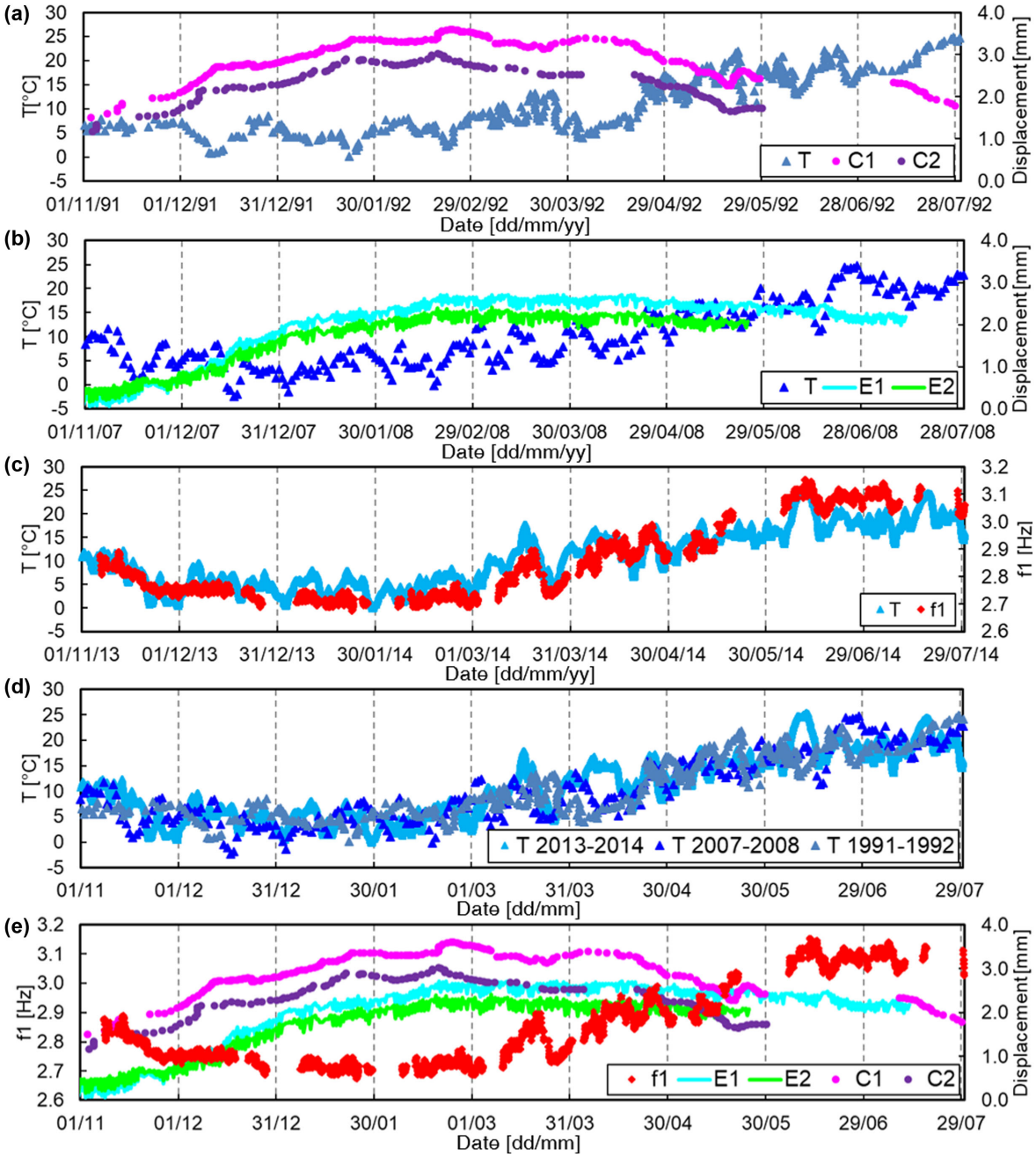

Figure 9. (a) Air temperature and measured displacements at crackmeters C1 and C2 on fractures F1 and F2 (1991 November–1992 July). (b) Air temperature and measured displacements at wire extensometers E1 and E2 on fracture $F4_1$ (2007 November–2008 July). (c) Measured air temperature and $f1$ values (2013 November–2014 July). (d) Overlapping temperature trends of the three monitored periods of (a)–(c). (e) Comparison between $f1$ values and all the available fracture opening/closing displacement measurements.

during warm periods A_{f3}/A_{f1} average value is lower than 0.5, while in cold months A_{f3} increases and it is higher than A_{f1} in several hours of recording, with A_{f3}/A_{f1} values up to 2. These spectral amplitudes globally confirm the thermal control on preferential directivity highlighted in the topographic data set. As already demonstrated for the fluctuations in resonance frequency values, also the temporal evolution of both noise spectral amplitudes and directivities seems therefore to be driven by temperature, with an alternating dominant effect of $f1$ and $f3$ in thermal contraction and expansion periods, respectively.

Even if these considerations are referred to the only compartment A, a more complete interpretation of the resonance frequencies recorded at the site is provided by the combined analysis of their values, spectral amplitudes and orientations over time. Thermal expansion of the rock mass causes relevant fracture closing. Consequently, during the warmest monitored hours or months, compartments A and B are reciprocally strongly constrained, slightly increasing the contact stiffness (K) but also the involved mass (M). With respect to eq. (1), this could explain the lowest frequency $f1$ (2.9 Hz) being dominant and describing the combined behaviour of

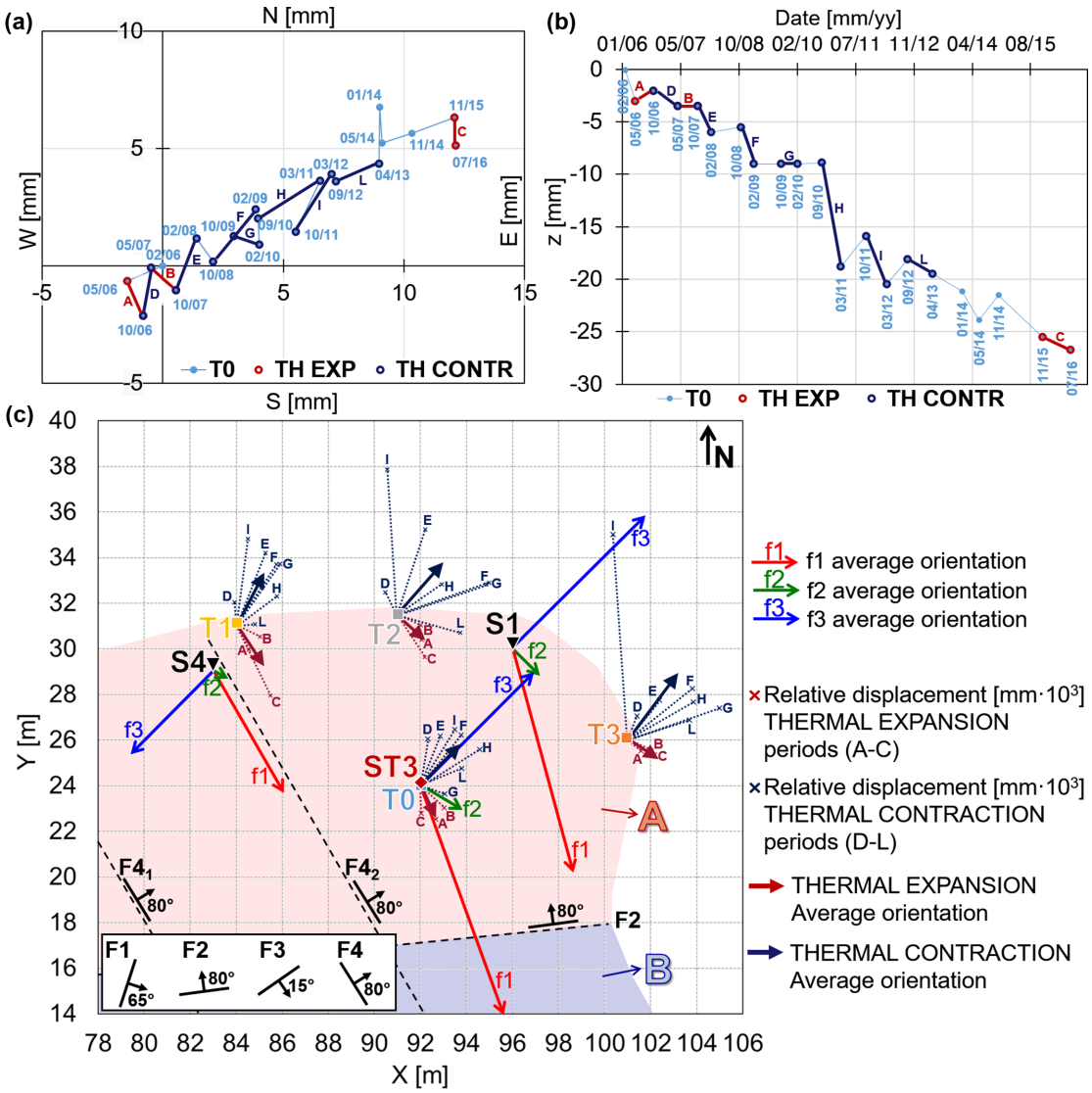

Figure 10. Topographic measurements (2006–2016) for the monitored point T0 (close to ST3) on (a) horizontal and (b) vertical planes. Basing on air temperature fluctuations, periods clearly dominated by thermal expansion (A–C) and contraction (D–L) between two subsequent measures are highlighted with dark red and dark blue segments, respectively. (c) Comparison in the horizontal plane between topographic and ambient noise spectral orientations on the unstable compartment A (fracture orientations are summarized in the white panel). Ambient noise monitoring stations (S1, S4 and ST3) report the orientation of the first three spectral peaks ($f1$, $f2$ and $f3$) obtained from 3-D ground motion estimation (Fig. 5d). Tips of each arrow mark the dip direction in the vertical plane, while lengths are proportional to the normalized spectral amplitudes. Relative displacements at each topographic station (T0–T3) during thermal expansion (A–C, dark red) and contraction (D–L, dark blue) periods are reported with the dashed lines (displacements [mm] are multiplied by 10^3). Average displacement orientations during thermal expansion/contraction are marked with dark red and blue bold arrows, respectively.

compartments A and B driven by thermal expansion. The convergent $f1$ orientations on compartments A and B, shown in Fig. 5(d), fully describe fracture closing due to thermal expansion and the consequent stronger coupling of A and B. The orientation of topographic displacements during thermal expansion periods confirms this hypothesis. Conversely, thermal contraction of the rock mass induces fracture opening and thus a relative decoupling of compartment A from compartment B. In this configuration, the two unstable blocks have weaker reciprocal constraints and behave in a more independent way. Basing on the temporal evolution of spectral amplitude and directivity of the resonance frequencies, $f3$ is likely the frequency describing the behaviour of the only compartment A, while $f2$ is the one related to compartment B, in the periods with dominant thermal contraction. Particularly, during these periods A_{f3} exceeds A_{f1} on compartment A, as resulting from the computed ratio and from the topographic data. In addition, looking at compartment A, the average orientation of $f3$ is perpendicular to the F4 fractures, with opposite dips on the two sides of $F4_2$, fully describing fracture opening in this direction. Assuming that $f2$ and $f3$ describe the behaviour of compartment B and A during cold months helps as well to understand the spectral amplitudes resulting from the temporary survey of ISTerre-Grenoble carried out in a cold period (end of 2010 November; S1–S6 in Fig. 5d). In detail, on compartment A, A_{f3} is on average 0.8 times A_{f1} at S1, and A_{f3} detected on S4 is really close to A_{f1}. Similarly, on compartment B, A_{f1} and A_{f2} are comparable at S3 and A_{f2} exceeds A_{f1} at S2, while A_{f3} is almost negligible. This predominant effect on amplitude of $f2$ and $f3$ is not detected at the long-term monitoring stations (ST1–ST4), since the related data are averaged over the whole monitored period (2013 November–2016 February). However, as shown in Fig. 5(b), $f3$ azimuthal variations

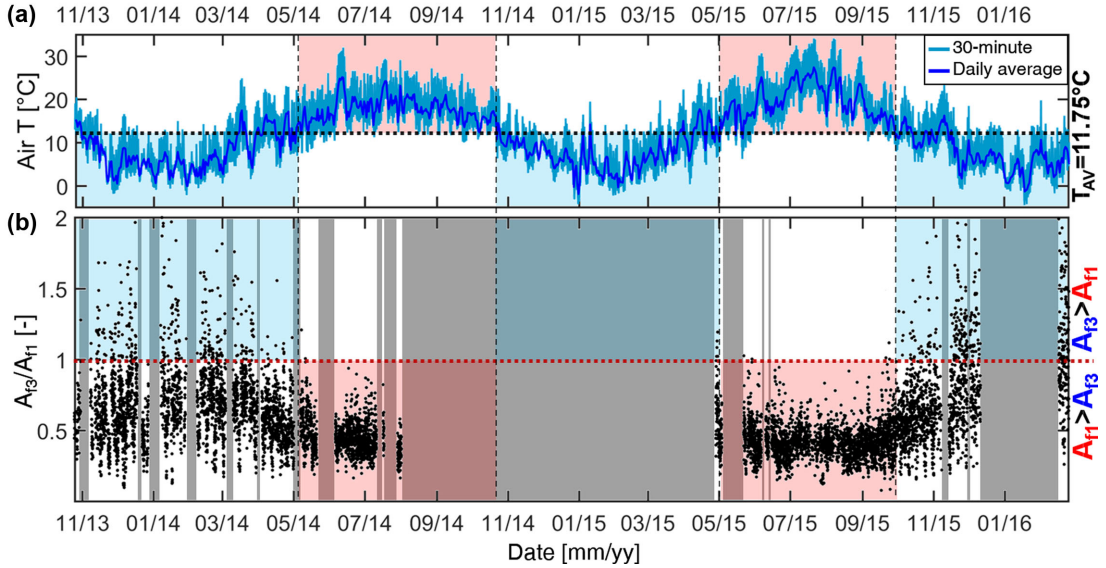

Figure 11. (a) 30-min and daily average air temperature fluctuations. (b) Hourly computed ratio between $f3$ and $f1$ spectral amplitudes measured at ST3 in the horizontal plane, over the whole monitored period. Warm and cold periods with daily temperatures, respectively, higher and lower than the average of the whole period (11.75 °C) are highlighted in red and blue on both plots. Periods with no monitoring data are shaded in grey.

recorded at ST3 are minimum in summer, when the related spectral amplitudes are the lowest, thus probably indicating a dominating effect of $f1$ also on directivities. Analogously, in the same period $f2$ azimuths tend to align to $f1$ orientation and show less marked short-period fluctuations.

6 CONCLUSIONS

This work was dedicated to the analysis of ambient noise temporal evolution on a complex unstable rock mass. To our knowledge, the study of Madonna delSasso is the first case of long-term noise monitoring with both spectral analysis and cross-correlation techniques, on a site with a complex 3-D fracture setting. Marked reversible daily and seasonal fluctuations were highlighted in resonance frequency values, as already found in previous noise studies on nearly 2-D rock columns. Cross-correlation results confirmed the same temporal modification in the seismic velocity field within the rock mass. These short- and long-term variations were interpreted as the result of a strong thermal control on the stability of the site. In contrast to the previous studies, reversible fluctuations in the resonance frequency values were found to be perfectly in phase with air temperature both at the daily and seasonal scale. This immediate response was linked to the bigger size of the studied unstable compartments and to a fracture-dominated stability behaviour, making thermal modification in the bulk rock properties a secondary issue with respect to the stiffness changes of fracture rock bridges. A direct linear relationship was established between temperature and resonance frequency values, offering the perspective to be introduced in a nearly real-time monitoring system for early warning purposes.

Further new perspectives of this study came from the long-term temporal analysis of noise spectral amplitudes and directivities. The strong temperature control was found to be the cause not only of fracture opening/closing (and thus of daily and seasonal frequency fluctuations and phase velocity changes within the rock mass) but of a general change in the dominant vibration directions of the unstable compartments. These were found to slightly change their reciprocal constraints, as well as the constraints to the stable cliff, according to thermal variations, with overlapping effects on the noise recordings related alternately to the single unstable compartments or to the whole unstable cliff. This interpretation was supported and confirmed by topographic displacement data.

Some limitations of this work have however to be taken into account for future improvements and perspectives. The availability of contemporary direct continuous displacement measurements on the site, even for temporary periods, could support a more systematic quantification of the real displacement associated to a certain change in the frequency value or amplitude of the spectral peaks, as well as to the modifications in the seismic velocity field. Longer and continuous seismic noise measurements are needed to reach a visible evaluation of the residual displacement, which is found to significantly accumulate over years from topographic measurements, but which influence on the spectral and velocity data sets is not clear in the available monitored period. Longer and continuous seismic noise measurements are needed, as well, to approach the final failure stages and to evaluate the critical phases of the collapse, in order to estimate the temporal gap between the drop in the value of the key monitored parameters and the final failure.

ACKNOWLEDGEMENTS

The long-term noise monitoring campaign of this study was funded within Progettod'Ateneo 2012—SAFER (Detecting slow deformation signals preceding dynamic failure: a new strategy for the mitigation of natural hazards) of Università degli Studi di Torino (grant number: TO_Call2_2012_0057). The ISTerre-Grenoble noise monitoring temporary survey was partially funded by the Interreg project MASSA (Medium And Small Size rock fall hazard Assessment) and the federal structure VOR-UGA (Vulnérabilité des Ouvrages aux Risques—Université Grenoble Alpes). Some of the used seismic instruments belong to the French national collection Sismob-RESIF. Authors are sincerely grateful to ARPA Piemonte and Regione Piemonte for the permission of publishing their monitoring displacement measurements and meteorological data.

REFERENCES

Bendat, J.S. & Piersol, A.G., 1971. *Random Data: Analysis and Measurement Procedures*, p. 407. Wiley, New York.

Bensen, G.D., Ritzwoller, M.H., Barmin, M.P., Levshin, A., Lin, F., Moschetti, M., Shapiro, N. & Yang, Y., 2007. Processing seismic ambient noise data to obtain reliable broad-band surface wave dispersion measurements, *Geophys. J. Int.,* **169**(3), 1239–1260.

Bottelin, P. *et al.*, 2013a. Spectral analysis of prone-to-fall rock compartments using ambient vibrations, *J. Environ. Eng. Geophys.,* **18**(4), 205–217.

Bottelin, P., Lévy, C., Baillet, L., Jongmans, D. & Guéguen, P., 2013b. Modal and thermal analysis of Les Arches unstable rock column (Vercors massif, French Alps), *Geophys. J. Int.,* **194**(2), 849–858.

Bottelin, P., Baillet, L., Larose, E., Jongmans, D., Hantz, D., Brenguier, O., Cadet, H. & Helmstetter, H., 2017. Monitoring rock reinforcement works with ambient vibrations: La Bourne case study (Vercors, France), *Eng. Geol.,* **226,** 136–145.

Burjánek, J., Gassner-Stamm, G., Poggi, V., Moore, J.R. & Fäh, D., 2010. Ambient vibration analysis of an unstable mountain slope, *Geophys. J. Int.,* **180**(2), 820–828.

Burjánek, J., Moore, J.R., Molina, F.X.Y. & Fäh, D., 2012. Instrumental evidence of normal mode rock slope vibration, *Geophys. J. Int.,* **188**(2), 559–569.

Colombero, C., Baillet, L., Comina, C., Jongmans, D. & Vinciguerra, S., 2017. Characterization of the 3-D fracture setting of an unstable rock mass: from surface and seismic investigations to numerical modeling, *J. geophys. Res.,* **122**(8), 6346–6366.

Colombero, C., Comina, C., Umili, G. & Vinciguerra, S., 2016. Multiscale geophysical characterization of an unstable rock mass, *Tectonophysics,* **675,** 275–289.

Curtis, A., Gerstoft, P., Sato, H., Snieder, R. & Wapenaar, K., 2006. Seismic interferometry—turning noise into signal, *Leading Edge,* **25,** 1082–1092.

Del Gaudio, V., Muscillo, S. & Wasowski, J., 2014. What we can learn about slope response to earthquakes from ambient noise analysis: an overview, *Eng. Geol.,* **182,** 182–200.

Derode, A., Larose, E., Tanter, M., de Rosny, J., Tourin, A., Campillo, M. & Flink, M., 2003. Recovering the Green's function from field-field correlations in an open scattering medium (L), *J. acoust. Soc. Am.,* **113,** 2973–2976.

Hadziioannou, C., Larose, E., Coutant, O., Roux, P. & Campillo, M., 2009. Stability of monitoring weak changes in multiply scattering media with ambient noise correlation: laboratory experiments, *J. acoust. Soc. Am.,* **125,** 3688–3695.

Konno, K. & Ohmachi, T., 1998. Ground-motion characteristics estimated from spectral ratio between horizontal and vertical components of microtremor, *Bull. seism. Soc. Am.,* **88,** 228–241.

Lacroix, P. & Helmstetter, A., 2011. Location of seismic signals associated with microearthquakes and rockfalls on the Sechilienne Landslide, French Alps, *Bull. seism. Soc. Am.,* **101,** 341–353.

Larose, E., Derode, A., Clorennec, D., Margerin, L. & Campillo, M., 2005. Passive retrieval of Rayleigh waves in disordered elastic media, *Phys. Rev.,* **E72,** 046607. doi:10.1103/physreve.72.046607.

Larose, E. & Hall, S., 2009. Monitoring stress related velocity variation in concrete with a 2×10^{-5} relative resolution using diffuse ultrasound, *J. acoust. Soc. Am.,* **125,** 1853–1856.

Larose, E. *et al.*, 2015. Environmental seismology: what can we learn on earth surface processes with ambient noise? *J. appl. geophys.,* **116,** 62–74.

Lévy, C., Baillet, L., Jongmans, D., Mourot, P. & Hantz, D., 2010. Dynamic response of the Chamousset rock column (Western Alps, France), *J. geophys. Res.*, doi:10.1029/2009jf001606.

Lévy, C., Jongmans, D. & Baillet, L., 2011. Analysis of seismic signals recorded on a prone-to-fall rock column (Vercors massif, French Alps), *Geophys. J. Int.,* **186,** 296–310.

Mainsant, G., Larose, E., Brönnimann, C., Michoud, C. & Jongmans, D., 2012. Ambient seismic noise monitoring of a clay landslide: toward failure prediction, *J. geophys. Res.*, doi:10.1029/2011jf002159.

McNamara, D.E. & Buland, R.P., 2004. Ambient noise levels in the continental United States, *Bull. seism. Soc. Am.,* **94,** 1517–1527.

Moore, J.R., Gischig, V., Burjanek, J., Loew, S. & Fäh, D., 2011. Site effects in unstable rock slopes: dynamic behavior of the Randa instability (Switzerland), *Bull. seism. Soc. Am.,* **101,** 3110–3116.

Paul, A., Campillo, M., Margerin, L., Larose, E. & Derode, A., 2005. Empirical synthesis of time-asymmetrical Green functions from the correlation of coda waves, *J. geophys. Res.*, doi:10.1029/2004jb003521.

Peterson, J., 1993. *Observations and modeling of background seismic noise*. Open-file report 93–322, U.S. Geological Survey, Albuquerque, New Mexico, p. 95.

Regione Piemonte, 1993. La rete di controllodellarupe di Madonna del Sasso, sintesideirisultatideiprimi 18 mesi di misure. AssessoratoDifesadelSuolo e GovernoRisorseIdriche. Settore per la prevenzionedelrischiogeologico, meteorologico e sismico. Servizio interventiprogettualigeologico-tecnici, pronto intervento e verificagrandiopereinfrastrutturali, Technical Report 52.

Sabra, K.G., Roux, P. & Kuperman, W.A., 2005. Arrival-time structure of the time-averaged ambient noise cross-correlation function in an oceanic waveguide, *J. acoust. Soc. Am.,* **117,** 164–174.

Sato, H., 2009. Green's function retrieval from the CCF of coda waves in a scattering medium, *Geophys. J. Int.,* **179,** 1580–1583.

Sens-Schönfelder, C. & Wegler, U., 2006. Passive image interferometry and seasonal variations of seismic velocities at Merapi Volcano, Indonesia, *Geophys. Res. Lett.,* **33**. doi:10.1029/2006gl027797.

Shapiro, N.M. & Campillo, M., 2004. Emergence of broadband Rayleigh waves from correlations of the ambient seismic noise, *Geophys. Res. Lett.,* **31**, doi:10.1029/2004gl019491.

Snieder, R., 2004. Extracting the Green's function from the correlation of coda waves: a derivation based on stationary phase, *Phys. Rev.,* **E69,** 046610, 1–8.

Spillmann, T., Maurer, H., Green, A.G., Heincke, B., Willenberg, H. & Husen, S., 2007. Microseismic investigation of an unstable mountain slope in the Swiss Alps, *J. geophys. Res.,* **112,** B07301, doi:10.1029/2006jb004723.

Tsai, V.C., 2011. A model for seasonal changes in GPS positions and seismic wave speeds due to thermoelastic and hydrologic variations, *J. geophys. Res.,* **116,** B04404, doi:10.1029/2010JB008156.

Valentin, J., Capron, A., Jongmans, D., Baillet, L., Bottelin, P., Donze, F., Larose, E. & Mangeney, A., 2017. The dynamic response of prone-to-fall columns to ambient vibrations: comparison between measurements and numerical modelling, *Geophys. J. Int.,* **208,** 1058–1076.

Wapenaar, K., 2004. Retrieving the elastodynamicgreen's function of an arbitrary inhomogeneous medium by cross correlation, *Phys. Rev. Lett.,* **93,** 254301, doi:10.1103/physrevlett.93.254301.

Weaver, R.L. & Lobkis, O.I., 2001. Ultrasonics without a source: thermal fluctuation correlations at mhz frequencies, *Phys. Rev. Lett.,* **87,** 134301, doi:10.1103/physrevlett.87.134301.

Xia, Y., Xu, Y.-L., Wei, Z.-L., Zhu, H.-P. & Zhou, X.-Q., 2011. Variation of structural vibration characteristics versus non-uniform temperature distribution, *Eng. Struct.,* **33,** 146–153.

APPENDIX A: NOISE CROSS-CORRELATION RESULTS

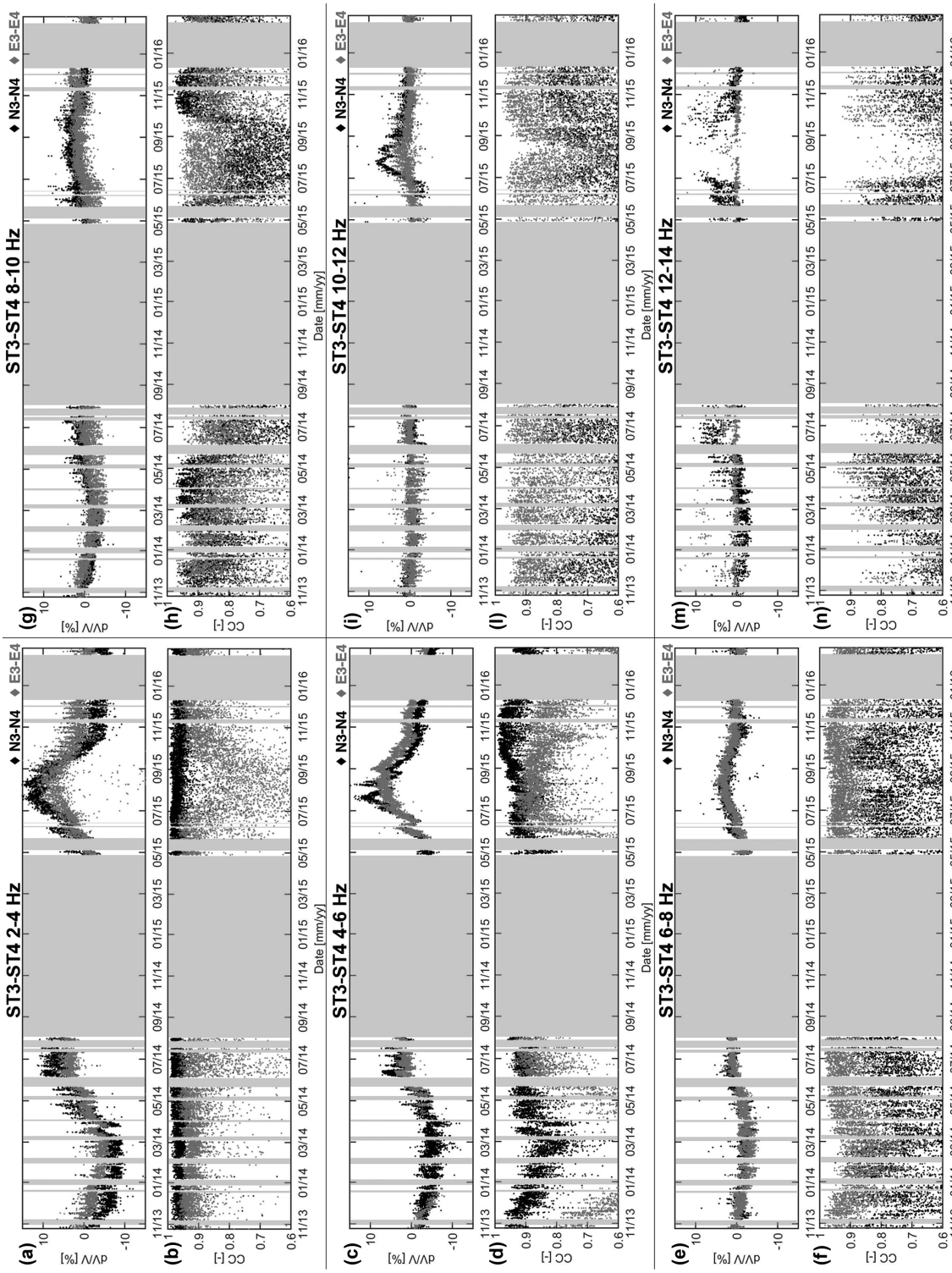

Figure A1. Hourly cross-correlations results between ST3 and ST4 horizontal components, in the tested 2-Hz frequency bands: (a) and (b) 2–4 Hz; (c) and (d) 4–6 Hz; (e) and (f) 6–8 Hz; (g) and (h) 8–10 Hz; (i)–(l) 10–12 Hz; (m) and (n) 12–14 Hz. (a), (c), (e), (g), (i) and (m) Relative velocity change (dV/V). (b), (d), (f), (h), (l) and (n) Cross-correlation coefficient (CC). Only results with CC > 0.6 are shown.

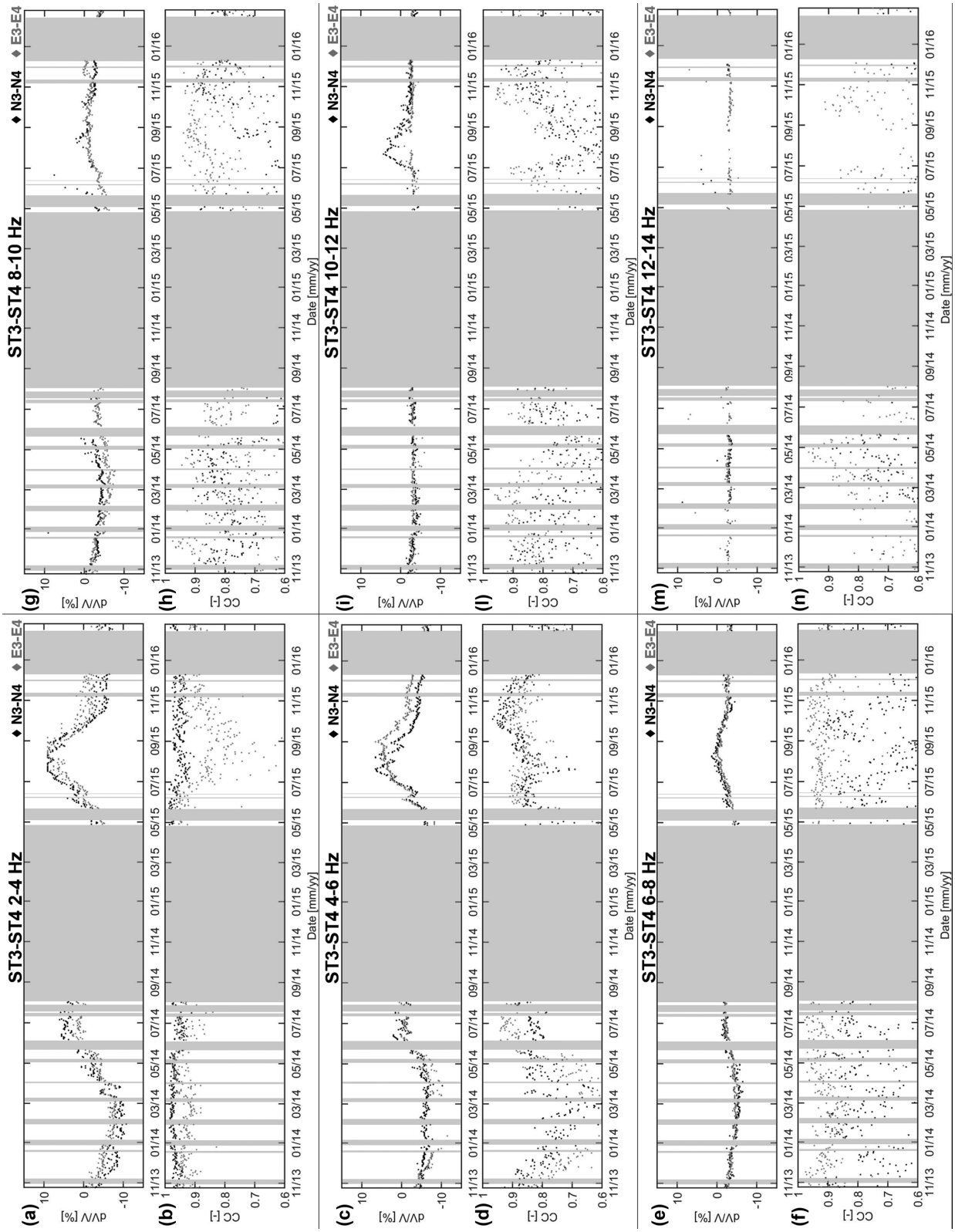

Figure A2. Daily cross-correlations results between ST3 and ST4 horizontal components, in the tested 2-Hz frequency bands: (a) and (b) 2–4 Hz; (c) and (d) 4–6 Hz; (e) and (f) 6–8 Hz; (g) and (h) 8–10 Hz; (i)–(l) 10–12 Hz; (m) and (n) 12–14 Hz. (a), (c), (e), (g), (i) and (m) Relative velocity change (dV/V). (b), (d), (f), (h), (l) and (n) Cross-correlation coefficient (CC). Only results with CC > 0.6 are shown.

APPENDIX B: TOPOGRAPHIC MEASUREMENTS

Table B1. Topographic measurements (2006–2016) acquired by ARPA Piemonte.

Date [dd/mm/yy]	T0			T1			T2			T3		
	x [mm]	y [mm]	z [mm]	x [mm]	y [mm]	z [mm]	x [mm]	y [mm]	z [mm]	x [mm]	y [mm]	z [mm]
08/02/06	0.0	0.0	0.0	0.0	0.0	0.0	0.00	0.00	0.0	0.0	0.0	0.0
05/05/06	−1.5	−0.7	−3.0	−0.4	−1.1	−1.0	-0.38	-0.51	-2.0	0.2	−2.0	−2.5
09/10/06	−0.8	−2.1	−2.0	0.2	−1.5	0.0	0.65	-1.48	-1.5	0.8	−3.0	1.5
03/05/07	−0.5	−0.1	−3.5	0.6	−0.5	−2.5	0.12	-0.49	-2.5	0.7	−2.0	−0.5
20/10/07	0.5	−1.0	−3.5	1.6	−0.9	−2.5	1.14	-0.96	-3.0	1.7	−2.4	−0.5
12/02/08	1.4	1.2	−6.0	3.0	0.8	−4.5	2.34	2.79	-5.5	3.0	0.8	−2.5
25/10/08	2.1	0.2	−5.5	2.1	0.7	−6.0	2.01	2.29	-6.0	3.3	−1.7	−5.5
13/02/09	3.9	2.4	−9.0	4.9	3.0	−9.0	5.86	3.62	-9.5	5.1	1.0	−8.5
06/10/09	2.9	1.3	−9.0	4.4	1.4	−8.5	3.91	2.40	-8.5	4.2	−1.6	−7.5
23/02/10	4.0	0.9	−9.0	8.4	2.8	−11.5	7.90	3.80	-10.0	6.1	1.1	−11.5
21/09/10	4.0	2.0	−8.9	6.3	2.2	−14.9	6.01	4.34	-14.6	5.6	−0.5	−5.8
02/03/11	6.5	3.6	−18.8	9.2	3.9	−19.3	7.94	5.66	-18.6	7.4	0.9	−17.7
03/10/11	5.5	1.4	−15.9	10.9	−4.7	−16.6	8.91	-0.61	-15.0	7.5	−3.3	−17.8
30/03/12	7.0	3.9	−20.4	10.3	4.3	−21.3	8.47	5.76	-20.8	8.0	0.5	−22.9
25/09/12	7.2	3.6	−18.1	9.9	4.5	−19.3	8.57	7.25	-22.2	9.3	1.2	−14.4
22/04/13	9.0	4.4	−19.5	12.6	5.4	−20.6	11.30	6.47	-19.4	10.1	1.3	−17.2
03/01/14	9.0	6.8	−21.1	12.7	6.7	−22.7	10.58	9.55	-25.6	10.1	3.9	−20.0
29/05/14	9.1	5.2	−23.9	13.1	6.4	−25.3	11.71	7.96	-24.2	10.0	1.0	−26.3
13/11/14	10.3	5.7	−21.5	13.7	6.2	−23.9	12.42	9.91	-25.9	11.5	1.0	−20.1
25/11/15	12.1	6.3	−25.5	15.5	7.2	−32.0	16.67	12.39	-25.8	13.1	2.2	−24.0
21/07/16	12.1	5.1	−26.7	16.6	6.5	−29.3	17.85	10.52	-26.8	14.6	−0.8	−24.1

Notes: Average displacements along *x*-, *y*- and *z*-directions (mm) at the monitoring points T0, T1, T2 and T3. Data correspond to the average values of measurements performed from the reference points T_{R1} and T_{R2} [location of all the topographic points is shown in Figs 1(c) and (d)].

Table B2. Couples of topographic measurements related to thermal expansion (A–C) or contraction (D–L) periods on the basis of dominant temperature increase or decrease within the period.

	PERIOD		T0				T1			
THERMAL EXPANSION (fracture closing)	Reference letter	Dates [dd/mm/yy]	Δx [mm]	Δy [mm]	Δz [mm]	Az [°]	Δx [mm]	Δy [mm]	Δz [mm]	Az [°]
	A	05/05/06-09/10/06	0.66	−1.47	1.00	156	0.54	−1.03	4.00	152
	B	03/05/07-20/10/07	1.04	−0.96	0.00	133	1.02	−0.47	0.00	115
	C	25/11/15-21/07/16	0.04	−1.20	−1.22	178	1.49	−3.04	−0.08	154
	Average displacement		**0.58**	**−1.21**	**−0.08**	**156**	**1.02**	**−1.51**	**1.31**	**140**
	PERIOD		T2				T3			
	Reference letter	Dates [dd/mm/yy]	Δx [mm]	Δy [mm]	Δz [mm]	Az [°]	Δx [mm]	Δy [mm]	Δz [mm]	Az [°]
	A	05/05/06-09/10/06	1.03	−0.97	0.50	133	0.57	−0.48	1.00	130
	B	03/05/07-20/10/07	1.01	−0.46	−0.50	115	1.02	−0.47	0.00	115
	C	25/11/15-21/07/16	1.18	−1.87	−1.00	148	1.18	−0.65	2.70	119
	Average displacement		**1.07**	**−1.10**	**−0.33**	**132**	**0.92**	**−0.53**	**1.23**	**121**
	PERIOD		T0				T1			
THERMAL CONTRACTION (fracture opening)	Reference letter	Dates [dd/mm/yy]	Δx [mm]	Δy [mm]	Δz [mm]	Az [°]	Δx [mm]	Δy [mm]	Δz [mm]	Az [°]
	D	09/10/06-03/05/07	0.32	2.06	−1.50	10	−0.09	1.04	−2.00	5
	E	20/10/07-12/02/08	0.87	2.18	−2.50	22	1.28	3.20	−2.00	22
	F	25/10/08-13/02/09	1.76	2.21	−3.50	39	1.74	2.71	−3.00	33
	G	06/10/09-23/02/10	1.06	−0.35	0.00	71	1.90	2.73	−4.00	35
	H	21/09/10-02/03/11	2.57	1.60	−9.92	58	1.75	1.30	−11.8	53
	I	03/10/11-30/03/12	1.48	2.46	−4.55	31	0.51	3.81	−5.16	8
	L	25/09/12-22/04/13	1.79	0.77	−1.36	67	0.82	0.08	−2.85	84
	Average displacement		**1.41**	**1.56**	**−3.33**	**43**	**1.13**	**2.13**	**−4.41**	**34**
	PERIOD		T2				T3			
	Reference letter	Dates [dd/mm/yy]	Δx [mm]	Δy [mm]	Δz [mm]	Az [°]	Δx [mm]	Δy [mm]	Δz [mm]	Az [°]
	D	09/10/06-03/05/07	−0.53	0.98	−1.00	28	0.40	1.06	−2.50	21
	E	20/10/07-12/02/08	1.21	3.74	−2.50	18	1.37	1.76	−2.00	38
	F	25/10/08-13/02/09	3.84	1.33	−3.50	71	2.81	2.25	−3.00	51
	G	06/10/09-23/02/10	3.99	1.40	−1.50	71	4.00	1.40	−3.00	71
	H	21/09/10-02/03/11	1.92	1.32	−4.02	55	2.86	1.67	−4.41	60
	I	03/10/11-30/03/12	−0.44	6.37	−5.83	4	−0.64	9.01	−4.64	4
	L	25/09/12-22/04/13	2.73	−0.78	2.76	74	2.69	0.88	−1.27	72
	Average displacement		**1.82**	**2.05**	**-2.23**	**46**	**1.93**	**2.58**	**−2.98**	**45**

Notes: For each period, the relative displacement (mm) between the second and first topographic measurements is calculated at all the topographic monitoring points (T0–T3) along *x*-, *y*- and *z*-directions (Δ*x*, Δ*y* and Δ*z*, respectively). The related azimuth (degrees from N direction) in the horizontal plane is computed for each period (*Az*) for further comparison with resonance frequency vibration directions. Average values of both displacements and azimuthal angles are reported in bold (at the end of each column).